The Cryosphere Discuss., https://doi.org/10.5194/tc-2018-74
Manuscript under review for journal The Cryosphere
Discussion started: 17 May 2018

The Cryosphere Discussions
Open Access
EGU

Basal control of supraglacial meltwater catchments on the Greenland Ice Sheet

Josh Crozier[1], Leif Karlstrom[1], and Kang Yang[2]

[1]University of Oregon Department of Earth Sciences, Eugene, Oregon, USA
[2]Nanjing University, Nanjing, Jiangsu, China

Correspondence: Josh Crozier (crozierjosh1@gmail.com)

Abstract. Ice surface topography controls the primary routing of surface meltwater on ablation zones of glaciers and ice sheets. Meltwater routing is important for understanding and predicting ice sheet evolution because surface melt can be both a direct source of ice mass loss and an influence on basal sliding and ice advection. Although controls on ice sheet topography at continental-scales are known, controls on the topographic features that influence meltwater routing at drainage basin scales (< 10s of km) are not well understood. Here we examine the effects of two processes that can influence ice sheet surface topography: basal transfer (where ice advection over variable bed topography and basal sliding conditions creates surface expressions), and thermal-fluvial incision (thermal erosion by supraglacial streams). We implement 2D bed topography and basal sliding transfer functions in seven study regions of the western Greenland Ice Sheet (GIS) ablation zone to study the influence of basal conditions on ice surface topography. Although bed elevation data quality is spatially variable, we find that ∼1-10 km scale ice surface features under variable ice thickness, velocity, and surface slope are well predicted by these transfer functions. We then use flow-routing algorithms to extract supraglacial stream networks from 2-5 m resolution digital elevation models, and compare these with synthetic flow networks calculated on ice surfaces predicted by bed topography transfer. Quantitative comparison of these networks reveals that bed topography can explain ∼1-10km surface meltwater routing patterns without significant contributions from thermal-fluvial erosion by streams. We predict how supraglacial internally drained catchment (IDC) patterns on the GIS would change under time-varying ice flow and/or basal sliding regimes. Basal sliding variations exert a significant influence on IDC spatial distribution, and suggest a potential positive feedback between subglacial hydrologic regime to surface IDC patterning. Increased basal sliding will increase IDC spatial density (by decreasing IDC sizes) and cause more disperse meltwater input to the englacial and subglacial environment. This could result in less efficient subglacial channelization and increased basal sliding that would then further increase IDC density.

The Cryosphere Discuss., https://doi.org/10.5194/tc-2018-74
Manuscript under review for journal The Cryosphere
Discussion started: 17 May 2018

1 Introduction

During warm seasons on the Greenland ice sheet (GIS) ablation zone, surface melting generates a large volume of water. Some meltwater is stored in or flows through porous firn (compacted snow), but most flows across the ice surface in supraglacial streams (Fountain and Walder, 1998; van den Broeke et al., 2009; Andersen et al., 2015; Meyer and Hewitt, 2017). The majority of these streams feed into the subglacial hydrological system either by flowing directly through open moulins or by flowing into supraglacial lakes (e.g., Chu, 2014; Smith et al., 2015; Yang and Smith, 2016; Smith et al., 2017), which can drain when enough water pressure builds up to fracture the ice (Das et al., 2008; Selmes et al., 2011; Stevens et al., 2015). Much of the meltwater will ultimately end up in the ocean after flowing through the englacial and subglacial hydrological systems (Enderlin et al., 2014; Andersen et al., 2015). Subglacial water significantly influences ice advection by reducing basal sliding resistance, though spatial and temporal water flux are important since the morphology of subglacial hydrologic pathways exerts a strong influence on sliding (e.g., Zwally et al., 2002; Schoof, 2010; Sole et al., 2011; Shannon et al., 2013). Processes associated with the spatial and temporal flux of surface meltwater to the subglacial hydrological system, which dictate how this flux evolves with changing climate and/or ice flow, are poorly constrained and largely not incorporated into current ice sheet mass balance models (Larour et al., 2012; Gillet-Chaulet et al., 2012; Gagliardini et al., 2013; Lipscomb et al., 2013; Khan et al., 2015; Smith et al., 2017).

Ice sheet surface meltwater flows downhill as dictated by surface topography. The largest scale of GIS topography is a continental-scale gravity current profile, where average surface slope is very gradual in the interior of the ice sheet and steepens approaching the margins (Cuffey and Paterson, 2010). Deviations from this geometry at smaller wavelengths however reflect a combination of other processes. Some are products of the surface energy balance, such as solar radiation-driven ice melting/sublimation, melting of ice by flowing surface water (we will refer to this process as thermal-fluvial incision), and snow accumulation (Cuffey and Paterson, 2010; Karlstrom and Yang, 2016; Boisvert et al., 2017; Meyer and Hewitt, 2017). Others are products of ice advection such as crevassing (Echelmeyer et al., 1991; Cuffey and Paterson, 2010) and propagating ice flux waves (Weertman, 1958; Nye, 1960; van de Wal and Oerlemans, 1995; Hewitt and Fowler, 2008). Still others involve the transfer of spatially variable bed topography, basal sliding, and ice rheology (due to temperature, grain alignment, impurities) to the surface (Gudmundsson, 2003; Raymond and Gudmundsson, 2009; Sergienko, 2013; Graham et al., 2017).

The advection of ice over rough bed topography (Fig. 1.A) (De Rydt et al., 2013; Yang and Smith, 2016) is thought to be a significant source of IDC scale (∼1-10 km) ice surface topography. Supraglacial IDC and lake locations generally remain fixed year to year despite ice advection, which suggests a basal controlling process (Lampkin, 2011; Lampkin and van der Berg, 2011; Selmes et al., 2011; Sergienko, 2013; Ádám Ignéczi et al., 2016; Karlstrom and Yang, 2016). We use the term "bed" loosely to refer to whatever material composes the substrate under an ice sheet. In many locations the bed contains a deformable till layer which may not influence ice flow in the same way as rigid bedrock (Tulaczyk et al., 2000; Cuffey and Paterson, 2010), and even rigid bedrock erodes under the action of ice motion (Sugden, 1978; Hart, 1995).

Thermal-fluvial incision is also important for the evolution of surface topography and meltwater channel networks (Parker, 1975; Karlstrom and Yang, 2016). Some supraglacial stream channels reform yearly as previous channels are advected by ice

The Cryosphere Discuss., https://doi.org/10.5194/tc-2018-74
Manuscript under review for journal The Cryosphere
Discussion started: 17 May 2018

flow, though other channels are reused for multiple years (Karlstrom and Yang, 2016). Stream channels can be meters deep, and are in places observed to flow in directions not parallel to the surrounding ice surface slope or to slice through topographic ridges altogether (Smith et al., 2015; Yang et al., 2015). Karlstrom and Yang (2016) suggested that longitudinal elevation profiles of supraglacial streams might even be inverted for primary production rate of meltwater, the analog to inferring tectonics from river profiles in terrestrial settings. However, although thermal-fluvial incision is required to make channels in the first place (e.g., lowering rate in channels must be greater than surroundings, Parker, 1975), it is unclear whether dynamic stream incision is efficient enough compared to other topographic influences to influence IDC-scale topography and meltwater routing. Supraclacial streams in this way may be more analogous to ephemeral gullies on earth flows (Mackey and Roering, 2011) than to river networks.

Understanding the processes that govern ablation zone surface topography could yield better means of tracking/predicting the spatial and temporal generation and routing of meltwater. Ice velocity, high resolution ice surface imagery and elevation models, and bed elevation datasets are now concurrently available over large expanses of the Greenland ice sheet (GIS) ablation zone (ArcticDEM, 2017; Joughin et al., 2010b, a; Helm et al., 2014; Morlighem et al., 2014, 2015, 2017; Nagler et al., 2015; Noel et al., 2015). With these data sets, we examine the significance and effects of bed topography transfer and thermal-fluvial incision on ice sheet surface topography and meltwater routing. We implement approximate analytical solutions for bed topography transfer through ice (Gudmundsson, 2003) to evaluate the extent to which bed topography transfer explains the ice surface in different flow regimes. To examine supraglacial meltwater routing we apply flow routing algorithms both to the real ice surface and to synthetic surfaces predicted from bed topography transfer. In the resulting flow networks we examine slope versus drainage area trends and flow network conformity to various wavelengths of surrounding ice surface topography. We identify bed topography transfer as a primary control on meltwater routing, and then use bed topography transfer functions to predict the response of GIS IDCs to changing ice flow conditions.

2 Methods

2.1 Data

We use stereo imagery derived SETSM ArcticDEM 2-5 m resolution mosaics for 2011 Greenland Ice Sheet (GIS) surface elevation (ArcticDEM, 2017; Noh and Howat, 2015). These DEMs were created by piecing together smaller DEM strips that in some cases come from data taken over multiple months, a potential source of error in our analysis since ice sheet surface topography can vary temporally due to a variety of processes including horizontal ice advection (on the order of 100 m/yr, (Joughin et al., 2010b, a; Nagler et al., 2015)), ablation (on the order of 1 m/yr (Bartholomew et al., 2011)), accumulation (on the order of 1 m/yr (Koenig et al., 2016)), and advection-related thickening/thinning such as that caused by changes in basal properties (on the order of 1 m/yr (Das et al., 2008; Helm et al., 2014)). We observe < 1 m vertical and < 10 m horizontal offsets from surface DEM stitching. We use the Icebridge BedMachine 150 m resolution Greenland bed elevation DEM (Morlighem et al., 2014, 2015), which is derived from radar and ice mass conservation modeling. This product has very high error (as much as 500 m) in areas with low radar pass density, which we take into account when selecting regions for our study. We

The Cryosphere Discuss., https://doi.org/10.5194/tc-2018-74
Manuscript under review for journal The Cryosphere
Discussion started: 17 May 2018

use 2009 InSAR derived MEaSUREs (Joughin et al., 2010b, a) and 2015 optical/SAR derived CCI Sentinel-1 (Nagler et al., 2015) (both data sets are 500 m resolution) for GIS surface velocities. We use Landsat imagery to identify moulins, lakes, and stream channels. We use RACMO 2.3p2 at 1 km resolution for melt data from the full year 2015 (Noel et al., 2015) to indicate relative melting between different regions of the GIS. All data sets do not necessarily correspond temporally, which is a potential source of error in our analysis since ice velocity, ice surface topography, and bed topography can vary temporally (Sugden, 1978; Hart, 1995; Bartholomew et al., 2011; Sole et al., 2011; Helm et al., 2014).

2.2 Study regions

We focus on areas of the GIS ablation zones that exhibit significant supraglacial drainage networks, that are not heavily crevassed (since dense crevassing can interfere with supraglacial drainage network development), and that do not contain ice streams (since ice streams often have very different ice advection and basal sliding properties than the surrounding regions of an ice sheet, and also often have heavily crevassed surfaces). Using these criteria we select seven internally drained catchments (IDCs) from the western GIS as primary study regions (Fig. 1.A, Table 1). These regions cover a significant fraction of the elevations, ice thicknesses, ice surface slopes, and ice surface velocities over which supraglacial stream networks form (Fig. 1.A). We also examine control region RSF from the eastern GIS that does not exhibit supraglacial streams (Fig. 1.A). For implementing bed topography transfer functions we primarily focus on regions R1 and R2 which exhibit near-uniform surface velocity and accurate bed DEMs, for reasons discussed in sections 2.3.1 and 2.3.2.

2.3 Bed topography and basal sliding transfer

2.3.1 Transfer function derivation

The governing equations of flowing ice are the Stokes equations for conservation of momentum and mass balance for an incompressible fluid. Though ice is better described with a nonlinear constitutive relation know as Glen's law (Cuffey and Paterson, 2010), here a linear Newtonian ice rheology is assumed. Ice rheology is also assumed to be spatially and temporally constant, though the rheology of ice generally varies with temperature, grain geometry, and sediment content. The momentum equations are then given by

$$\boldsymbol{\nabla} p = \eta \boldsymbol{\nabla}^2 \boldsymbol{u} + \rho_i \boldsymbol{g}, \tag{1}$$

where p is pressure, η is effective dynamic ice viscosity, $\boldsymbol{u}$ is ice velocity, and ρ_i is ice density. Cartesian coordinates are used, where the z-axis is aligned normal to the mean ice surface and the x-axis points in the direction of maximum bed gradient. $\boldsymbol{g}$ is the gravitational acceleration (in the $-z$ direction). Conservation of mass is given by

$$\boldsymbol{\nabla} \cdot \boldsymbol{u} = 0. \tag{2}$$

We use transfer functions derived by Gudmundsson (2003) to solve Eqs. (1) and (2) and predict ice surface topography over underlying rough bed topography or basal sliding variations. In the spectral domain, transfer functions are generally of

The Cryosphere Discuss., https://doi.org/10.5194/tc-2018-74
Manuscript under review for journal The Cryosphere
Discussion started: 17 May 2018

the form $\hat{Y}(\boldsymbol{k}) = \hat{X}(\boldsymbol{k})\hat{T}(\boldsymbol{k})$ where $\boldsymbol{k} = (k_x, k_y)$ is a wave-number (inverse wavelength) vector, Y is output data (ice surface elevation in our case), X is input data (bed elevation in our case), and T is the transfer function relating outputs to inputs. Transfer functions are possible to obtain for linear time-invariant systems; the basic underlying principals are that the output for such systems may be calculated for any single wave-number input, that any input may be represented as a sum of individual wave-number components via Fourier transform, and that the output will be a sum of the independent outputs from each input component (Stein and Wysession, 2005). In the rest of this section we will briefly describe the derivation of the transfer functions (described fully in (Gudmundsson, 2003)) and the important approximations made in this derivation.

Bed erosion is ignored and bed elevation is assumed to not change temporally beyond an initial perturbation. Basal melting/freezing are also ignored, assumptions that are likely reasonable from a mass conservation perspective due to the generally slow rates of basal melting/freezing (Huybrechts, 1996). Basal sliding velocity $\boldsymbol{u}_b$ is assumed to be governed by a sliding law of the form

$$\boldsymbol{u}_b(x,y) = C(x,y)\boldsymbol{\tau}_b(x,y) \tag{3}$$

where $\boldsymbol{\tau}_b$ is basal shear stress and C is a sliding parameter. We will often refer to non-dimensionalized basal sliding coefficient $C^* = C\frac{2\eta}{H}$ (approximately equivalent to slip ratio). Other forms of sliding law have been proposed (Fowler, 1986; Tulaczyk et al., 2000; Cuffey and Paterson, 2010). The basal boundary condition (at the bed surface) combines this sliding law with a no flow condition dictating zero ice velocity normal to the boundary. Surface accumulation/ablation are ignored, which is reasonable as both rates are generally small compared to ice advection rates (van den Broeke et al., 2011). The ice surface boundary conditions are zero traction plus the kinematic boundary condition

$$\frac{\partial Z}{\partial t} = u_z - u_x\frac{\partial Z}{\partial x} - u_y\frac{\partial Z}{\partial y}. \tag{4}$$

Thus the ice surface boundary is the only source of time variation in the system.

Parameters including ice thickness, surface velocity, and surface slope are assumed to be similar over the domain of interest, which allows for solutions to be obtained as perturbations to a zeroth-order infinite plane slab solution. In order for these assumptions to be valid, it is assumed that bed topography amplitude is much smaller than ice thickness, and that the domain of interest is small compared to the horizontal dimensions of the ice sheet. The zeroth-order ice surface Z^0 is a plane with slope α in the direction of ice flow. Zeroth-order ice thickness H is the mean ice thickness in the domain. Zeroth-order basal shear stress is given by $\tau_b = \rho g H \sin(\alpha)$, and zeroth-order deformational velocity is given by $U_d = \frac{1}{2\eta}\tau_b H$, where ρ is (spatially constant) ice density.

Bed elevation B is expressed as $B = B^0 + \epsilon F_B^\epsilon$, where B^0 is zeroth-order (horizontal plane) bed elevation, F_B^ϵ represents perturbations to B^0, and $\epsilon =$ bed topography amplitude$/H \ll 1$. Basal sliding coefficient C is similarly expressed as $C = C^0 + \beta F_C^\beta$ where $0 \leq \beta \ll 1$. Equations 1 and 2 are linearized around $\epsilon, \beta = 0$ and solved in the Fourier domain. Ice surface elevation is then given by

$$Z = Z^0 + \epsilon F_Z^\epsilon + \beta F_Z^\beta + \mathcal{O}(\epsilon^2, \beta^2, \epsilon\beta), \tag{5}$$

The Cryosphere Discuss., https://doi.org/10.5194/tc-2018-74
Manuscript under review for journal The Cryosphere
Discussion started: 17 May 2018

where ϵF_Z^{ϵ} and βF_Z^{β} represent the first order (linear) ice surface response to B and C perturbations. Higher order terms $\mathcal{O}(\epsilon^2, \beta^2, \epsilon\beta)$ are discarded.

The full time-dependent transfer functions from Gudmundsson (2003) are reproduced in Appendix A1. A steady state surface configuration to bed topography and basal sliding perturbations is approached as $t \rightarrow \infty$. We note that ice flow parameters in the transfer functions are not strictly independent, such that there are limited parameter combinations that produce realistic ice flow configurations.

The linear transfer functions derived by Gudmundsson (2003) (Appendix A1) do not capture all the complexities of ice motion, as discussed above. However, they have some significant advantages over other methods for solving ice flow problems. They do not make a shallow ice approximation (which ignores longitudinal stresses and thus breaks down at length scales on the order of ice thickness H (e.g., Cuffey and Paterson, 2010)), and are thus valid at spatial scales $< H$. Additionally, they can be efficiently implemented over 2D IDC-scale regions without requiring initial conditions and domain-edge boundary conditions that numerical flow simulators need. Although many of the assumptions made deriving these transfer functions are likely somewhat unrealistic over much of the GIS, we will show that the functions still reproduce general topographic features and amplitude spectra well, and provide a useful predictive tool.

2.3.2 Transfer function implementation

When implementing the transfer functions in all following analysis we will assume the ice surface has reached a steady state in response to the underlying bed topography and basal sliding conditions. To examine the validity this assumption, we calculate the transfer function perturbation adjustment timescales for parameters representative of the western GIS ablation zone (from study region R1 (Fig. 1.A, Table 1) with C^{0*} = 11 and η = 10^{14} Pa s) using the time-dependent transfer functions defined in Appendix A1. For the range of ice flow parameters we are interested in, there is no appreciable downstream advection of surface perturbations (Gudmundsson, 2003), and so the surface response soon after a basal perturbation is essentially a lower amplitude scaling of the steady state (maximum amplitude) surface response. We find that the time scale for bed topography or basal sliding transfer amplitudes to reach 95% of their steady state values is as much as 60 years for the longest wavelengths of topography in our typical study areas (∼20 km), and is ∼3-20 years for wavelengths that typically exhibit the highest transfer (∼1-10 km). It is probably unlikely that bed topography, ice sheet thickness, or ice sheet surface slope change significantly over these timescales, but ice velocity and basal sliding can vary on day to year timescales, meaning that the steady state assumption is a potential source of error in our analysis (Das et al., 2008; Bartholomew et al., 2011; Sole et al., 2011; Helm et al., 2014; Chandler et al., 2013).

To implement the transfer functions, rather than using coordinates aligned in the ice flow direction we use Cartesian coordinates aligned in the (east ,north, vertical) directions, thus $k = \|\boldsymbol{k}\|$ and $(k_U = \frac{\boldsymbol{k} \bullet \boldsymbol{U}}{\|\boldsymbol{U}\|}$. We can then calculate transfer function matrices $\left(\hat{T}_B(k_x, k_y)\right.$ and $\left.\hat{T}_C(k_x, k_y)\right)$ corresponding to the discrete wavenumber components of a given bed DEM (Fig. 2). Due to the alignment of k_U with the direction of ice flow, the amplitude matrix A is symmetric about the line perpendicular to this direction, and the phase matrix ϕ is anti-symmetric about the line perpendicular this direction. The transfer amplitude for bed topographic features aligned with the direction of ice flow approaches one as wavelength approaches infinity, but non-zero

The Cryosphere Discuss., https://doi.org/10.5194/tc-2018-74
Manuscript under review for journal The Cryosphere
Discussion started: 17 May 2018

values of the basal sliding parameter C^{0*} result in an additional peak in transfer amplitudes at intermediate wavelengths (Fig. 3, Gudmundsson, 2003). Transfer amplitudes approach zero at small wavelengths or as topographic features approach a flow-perpendicular alignment (Fig. 2). Transfer function phase shift is also important, and results in a wavelength-dependent offset between bed features and their surface expression (Fig. 5).

The two-dimensionality of the transfer functions is important. This can be demonstrated by examining a scenario with different single-wavenumber components of bed topography (plane-waves) that have the same apparent wavenumbers in a transect interpolated across bed topography along an ice flowline (a bed elevation profile along the ice flow direction). The same apparent wavenumber in the ice flow direction k_U could arise from any single wavenumber component of bed topography with absolute wavenumber $k = k_U \cos(\theta)$ aligned at angle θ from the ice flow direction, where the plane-wave ridge alignment is perpendicular to the direction of ice flow when $\theta = 0$. If we evaluate the predicted transfer functions for a given k_U and set $k = k_U \cos(\theta)$ for a range of θ, we can see that the transfer amplitude and phase both depend upon θ, even though the apparent flowline bed topography is the same for all $\theta \neq \frac{n\pi}{2}$ (see equations in Appendix A2). Thus the configuration of bed topography off of a flowline can influence the ice surface over said flowline. With ice flow parameters representative of the western GIS ablation zone, the predicted transfer amplitude of IDC-scale (∼1-10 km) bed features could vary by up to a factor of 10 depending upon the 2D alignment of those features. (Fig. 4).

Prior to taking 2D discrete Fourier transforms (DFTs, see Perron et al., 2008 for DFT definition) of bed DEMs, we first shift each bed DEM to have zero mean elevation. We do not detrend bed DEMs, as that is not consistent with the zeroth-order bed conditions. We then mirror each bed DEM in all directions by connecting east-west reversed copies of each DEM to the east and west sides of itself, connecting north-south reversed copies of each DEM to the north and south sides of itself, and connecting north-south and east-west reversed copies of each DEM to all corners of itself. Next we apply a cosine taper such that all elevations along the edges of each mirrored bed DEM are zero, and the original domain in the center is unaffected. These processing steps are taken to minimize edge effects (Perron et al., 2008). We then take 2D DFTs of the mirrored bed DEMs, and use the transfer functions to obtain predicted ice surface elevation Z' as:

$$Z'(x,y) = Z^0(x,y) + \mathcal{F}_D^{-1}\left(\hat{T}_B(k_x,k_y)\hat{B}(k_x,k_y) + \hat{T}_C(k_x,k_y)\hat{C}(k_x,k_y)\right) \quad (6)$$

where B is the zero-mean bed elevation, Z^0 is the zeroth-order ice surface (with average elevation H and slope α, obtained by a plane fit to the actual ice surface elevation Z), and $\mathcal{F}_D^{-1}$ represents the inverse 2D DFT (see Appendix A3). We then trim enough space from the edges of each predicted surface so that we are only considering a region that will not contain any artificial edge effects.

2.3.3 Ice viscosity and basal sliding estimation

Two important and poorly constrained parameters in our bed topography transfer method are ice viscosity η and basal sliding parameter C^*. One possible application of the transfer functions is to infer these parameters as a function of space from observed surface and bed DEMs (Raymond and Gudmundsson, 2009). We do not take this approach here. Rather, we are

The Cryosphere Discuss., https://doi.org/10.5194/tc-2018-74
Manuscript under review for journal The Cryosphere
Discussion started: 17 May 2018

concerned with a more basic assessment of how well ice surface topography can be explained by transfer of basal conditions. However, we do need to choose values for η and C^*.

We first focus on C^* by comparing the predicted ice surface over Gaussian B and C^* perturbations with 2 km standard deviations and 200 m height or 200 C^* amplitude, using ice flow parameters from region R1 (Fig. 1.A, Table 1) with $\eta = 10^{14}$ Pa s and $C^{0*} = 11$ for the Gaussian bed topography test case (Fig. 5). This qualitatively indicates that in these flow conditions unless C^* perturbations are very large, the ice surface response to C^* perturbations is of much smaller amplitude and more disperse than the surface response that can arise from reasonable amplitude bed topography. Since the predicted surface effects from C^* perturbations are generally relatively small in the range of ice flow conditions we are interested in, we assume spatially constant C^* (so $C^* = C^{0*}$ at all locations) for all analysis.

We next assess the uniqueness with which C^{0*} and η can be inverted for using the transfer functions. We do this by minimizing misfit $\left(\text{defining misfit \% as } 100\frac{(Z-Z')}{\text{Range}(Z)}\right)$ between observed and bed topography transfer predicted ice surfaces (Fig. 6). We do this over our seven study regions of the GIS ablation zone (Fig. 1.A, Table 1), and find that in regions with good conditions for applying the transfer functions (where bed DEM error is low and ice velocity is near-uniform), the values of viscosity that produce best fits between predicted and observed ice surfaces are within half an order of magnitude of 10^{14} Pa s, and the best fitting values of C^{0*} are between 8 and 20. For all further analysis we fix the value of η to 10^{14} Pa s, which is within the realm of commonly assumed values of ice viscosity (Cuffey and Paterson, 2010). Except where otherwise noted we fix the value of C^{0*} to 11, which is also similar to other ice sheet ablation zone estimates (Morlighem et al., 2013; MacGregor et al., 2016). We note that C^{0*} only affects the amplitude of bed topography transfer peaks and not the wavelengths over which these peaks occur (Fig. 3), so though C^{0*} is likely variable between regions this variability will not affect much of our analysis.

2.3.4 Bed DEM error analysis

A significant source of error in our bed topography transfer function method is bed DEM accuracy. The bed DEMs we use have corresponding error maps which represent the uncertainty in bed elevation values (Fig. 7). This uncertainty is primarily a result of incomplete radar transect coverage, requiring bed elevation in between transects to be modeled. Bed DEM error in this dataset generally depends upon ice velocity and distance from radar transects (Morlighem et al., 2014, 2015). We test the sensitivity of our transfer function to potential bed DEM error by injecting 100 randomly generated possible error configurations at each of 100 different wavelengths λ_n spanning the range of wavelengths resolvable in a given domain. Each error configuration is created by using a pseudo-random number generating algorithm to create a complex wavenumber matrix. Each wavenumber matrix has the same dimensions as the bed DEM, and has left-right mirrored halves such that real components are symmetric and imaginary components are anti-symmetric (where all real and imaginary components vary between -1 and 1). Each wavenumber matrix is then bandpass filtered by multiplication with a narrow Gaussian ring surface (a radially symmetric surface centered around zero wavenumber that along any radial transect is a Gaussian function centered at radius $\frac{1}{\lambda_n}$). An inverse DFT is then taken of each wavenumber matrix to create pseudo-random surfaces with amplitude spectral peaks at λ_n. Each surface is then scaled so that all values vary between -1 and 1, and then multiplied by the bed DEM error map to generate a possible error configuration. We then add each error configuration to the bed DEM and implement

the bed topography transfer function on each error-injected bed DEM, storing the surface prediction values from each error configuration. By using many randomly generated possible error configurations at a variety of wavelengths, we can assess the range of surface topography variation that is allowed by current bed DEM data quality.

2.3.5 Observed admittance of ice surface/bed topography

Given both bed and surface DEMs, we can calculate the spectral domain admittance of bed topographic features to ice surface topography. Admittance is given by $\hat{A}(k_x, k_y) = \hat{Z}(k_x, k_y)/\hat{B}(k_x, k_y)$, so if surface topography is only caused by bed topography transfer then admittance should correspond to the bed topography transfer function. However, limited DEM precision makes interpreting direct admittance computations and comparing them to transfer functions challenging. We thus employ two methods to examine admittance. One method is to take 2D discrete Fourier transforms (DFTs) of mirrored and tapered ice surface and bed DEMs (as described in Section 2.3.2), bin and average them by absolute wavenumber, then divide the binned wavenumber spectra to obtain 1D admittance. This method thus blends ice-flow-parallel and non-ice-flow-parallel topographic features, which could mute the admittance relative to admittance purely along ice flowlines. The second method is to interpolate bed elevations along a series of parallel ice flowlines, mirror and taper each flowline elevation profile, take DFTs of each bed profile, then bin and average the wavenumber spectra of all bed profiles. The same is done with ice surface elevation profiles, then the binned ice surface spectra is divided by bed spectra to obtain average flowline 1D admittance. This method thus avoids the non-ice-flow-parallel muting effect from the first method, but does not account for the effects of surrounding 2D topography on each flowline (as discussed in Section 2.3.2).

2.4 Meltwater routing

2.4.1 Supraglacial stream network extraction

We use satellite imagery, DEMs, and flow routing algorithms to extract supraglacial stream networks from seven regions of the western GIS ablation zone (Karlstrom and Yang, 2016; Yang and Smith, 2016) (Fig. 8). Satellite imagery is used to identify by hand moulins/lakes, which are treated as water sinks. We then use flow routing to calculate accumulated flow/drainage area patterns on the surface. We use the D8 (steepest descent) flow routing algorithm from ArcGIS with channel area threshold set to maximize agreement with visible stream channels, between 8000 and 30000 m^2 depending upon region. In general, flow routing is an imperfect means of finding real stream channels, especially on a relatively flat landscape such as the GIS. DEM resolution is not high enough to resolve narrow ($< \sim$2 m wide) supraglacial stream channels, so such streams may be missed by flow routing, particularly those that are not aligned with the steepest descent direction (Smith et al., 2015; Yang et al., 2015). However, most streams found via our flow routing method agree with visually identified stream channels (Karlstrom and Yang, 2016; Yang and Smith, 2016).

We employ two approaches to quantify the observed pattern of supraglacial stream networks in relation to ice flow and bed topography transfer. The first approach is to compare slope versus accumulated drainage/flow area relations (a traditional terrestrial landscape metric (Gilbert, 1877; Whipple and Tucker, 1999; Montgomery, 2001)) between real supraglacial stream

networks and synthetic flow networks on surfaces without streams (either stream-free regions of the GIS or bed topography transfer predicted surfaces). The second approach is to quantify how well supraglacial stream network geometry is explained by the surrounding ice surface and what topographic wavelengths are most important for this.

We create synthetic flow networks in two ways. We first compute synthetic flow pathways on a stream-free region of the GIS by placing artificial moulins (as water sinks) at the base of large depressions, then predicting flow pathways numerically. This method is complicated by the presence of few regions of the GIS differing only in the presence or absence of thermal-fluvial incision, and since moulins do not only occur in depressions (Catania et al., 2008; Yang et al., 2015; Yang and Smith, 2016). Bed topography transfer provides another way to construct synthetic stream networks. We use transfer functions to predict the ice surface over bed DEMs, then place artificial moulins at the base of large surface depressions and calculate synthetic flow networks numerically. We calculate all synthetic flow networks with the TopoToolbox (Schwanghart, 2014) D8 method, with channel area threshold set to 20000 m^2.

2.4.2 Slope versus drainage area and thermal-fluvial incision

Our first approach for quantifying controls on meltwater routing comes from the hypothesis that bed topography transfer can explain meltwater routing trajectories, without appealing to fluvial incision. If supraglacial stream incision is a primary control on ice surface topography at km scales, the interplay between thermal-fluvial erosion and ice flow will set the longitudinal profiles of streams and relationship between slope and accumulated flow/drainage area of streams networks (Karlstrom and Yang, 2016).

Modeling the transient competition between ice flow and thermal-fluvial incision is outside the scope of the present work. Instead, we use empirical metrics to compare the relation of slope to accumulated upstream flow/drainage area at all points in each stream network. Prior to doing this we smooth all stream longitudinal profiles to remove small-scale slope variations. Profile smoothing is done by first breaking each stream network into multiple separate stream profiles, discarding all profiles less than 800 m long, then twice applying a moving average filter with a span of 200 m (analogous to a lowpass filter with a 200 m wavelength threshold) to each remaining profile, and finally trimming 100 m from both ends of each profile to remove smoothing-induced edge effects. We then calculate stream longitudinal slopes with a 2nd order centered finite difference approximation. There is a large scatter in the resulting slope versus drainage area relations, so for each stream network we divide data points into logarithmically spaced area bins and calculate the average slope in each bin (Montgomery, 2001; Warren et al., 2004).

2.4.3 Supraglacial stream network topographic conformity

Our second approach for quantifying meltwater routing is to implement two regional measures of stream network conformity to surrounding ice surface topography devised by Black et al. (2017). This approach assesses the degree to which stream patterns are "explained by" the current configuration of surrounding ice surface topography at various wavelengths. Percent downhill ($\%d$) measures the percentage of the length along stream channels over which the streams are flowing downhill. Conformity factor (Λ) measures the mean deviation of stream channel paths from the direction of steepest descent on the ice surface. We

The Cryosphere Discuss., https://doi.org/10.5194/tc-2018-74
Manuscript under review for journal The Cryosphere
Discussion started: 17 May 2018

low-pass filter ice surface DEMs using a series of decreasing cutoff and taper wavelengths, then calculate percent downhill and stream conformity factor by projecting stream networks onto each filtered surface. With a perfect DEM, as filter cutoff wavelength approaches zero $\%d$ should generally increase and approach 100% since streams do not flow uphill. Similarly, Λ should generally increase and approach 1, since water should generally flow in the direction of steepest descent.

As filter cutoff wavelength increases both metrics will decrease if stream network geometry is controlled by the shorter wavelengths of topography that are being removed (Black et al., 2017). Such decreases in conformity might occur for a variety of reasons, for example if the wavelengths being removed encompass topographic features that predate stream formation and thus contributed to the routing of the stream channel when it formed. Conformity decreases could also occur at longer cutoff filter wavelengths if fluvially driven stream meanders have shifted channels away from the direction of steepest descent relative to background topography, or if background topography has been modified by processes such as ice advection (Black et al., 2017; Wegmann et al., 2007). We use the conformity metrics only to indicate what topographic wavelengths are important for explaining current supraglacial meltwater routing.

To calculate the two conformity metrics, we low-pass filter ice surface DEMs using one-sided Gaussian filters. Prior to filtering we apply pre-processing steps as described in Section 2.3.2 to minimize edge effects. We then project flow networks (as found on the unfiltered DEMs) onto the filtered surfaces. We calculate $\%d$ as the percent of discrete locations along stream channels that are higher in elevation than the next downstream locations along the same channels. To calculate Λ, at each discrete location along a stream we calculate the angle between the horizontal direction vector of the stream channel (the direction water is flowing) and the horizontal direction vector of steepest descent down the ice surface. Λ is then given by the mean absolute value of the cosine of this angle at all discrete stream channel locations. Exact expressions for $\%d$ and Λ are given in Appendix A4. We note that applying these conformity metrics to stream networks calculated with flow routing on imperfect DEMs may result in a bias towards artificially high conformity, since as mentioned in Section 2.4.1 flow routing may miss some narrow stream channels that are are not aligned with the steepest descent direction on the ice surface. However, since we have verified that flow routing properly captures the majority of stream network structure we expect that the general trends in conformity metrics observed with changing filter wavelengths will be valid.

2.5 Identifying ice surface topographic basins

We are interested in examining the response of IDCs to changing ice flow conditions using bed topography transfer predictions. To do this we extract topographic basins from predicted surface topography (as described in Section 2.3.2) over one example study region R1 (Fig. 1.A, Table 1) with various ice flow and basal sliding parameters. Topographic basins will not exactly correspond to IDCs, since moulins fragment topographic basins and/or there could be places where streams have incised through topographic divides (Smith et al., 2015; Yang et al., 2015; Yang and Smith, 2016), but in practice there is a reasonable correspondence between topographic basins and IDCs. We use flow routing as described in Section 2.4.1, with all topographic local minima treated as water sinks, to identify basin divides. All edge terminating topographic basins are counted separately.

The Cryosphere Discuss., https://doi.org/10.5194/tc-2018-74
Manuscript under review for journal The Cryosphere
Discussion started: 17 May 2018

3 Results

3.1 Bed topography transfer

We calculate observed admittance of bed topography to ice surface topography (as described in Section 2.3.5) in the seven study regions of the western GIS ablation zone. In all regions, admittance corresponds well to predicted bed topography transfer amplitudes (as described in Section 2.3.1) at wavelengths $>\sim$1 km (Fig. 9). Notably, admittance peaks appear at wavelengths from $\sim$1-10 km, as predicted by bed topography transfer functions.

We then use the steady-state bed topography transfer functions to predict the ice surface (as described in Section 2.3.2) in our seven study regions (Fig. 1.A, Table 1). We find that the transfer functions accurately predict surface relief and qualitatively well predict general IDC-scale ($\sim$1-10 km, consistent with our admittance calculations) features of the ice surface, such as large ridges and depressions (Fig. 7).

Admittance in all regions exhibit a significant discrepancy from bed topography transfer predictions at wavelengths $<\sim$1 km (Fig. 9). Misfit between the bed transfer predicted ice surfaces and ice surface DEMs is also often non-trivial, with mean misfit values of $\sim$8-16% of the surface topographic relief in each region (Fig. 7). As discussed in sections 2.3.1 and 2.3.2, there are many potential causes of these discrepancies including: bed DEM error, the various assumptions made in deriving and implementing the transfer functions (such as assuming Newtonian ice rheology, linearity, and a steady-state limit), and/or unaccounted for physics.

We use the approach described in Section 2.3.4 to examine the potential effects of bed DEM error on ice surface predictions in our study regions, and find that the potential effects of bed DEM error on ice surface predictions are significant, ranging from $\sim$40% to larger than 100% of regional ice surface relief depending upon the configuration and magnitude of DEM error. However, where bed DEMs are relatively accurate (generally less than $\sim$100 m error) these error effects are smaller than the regional ice surface relief (Fig. 7), indicating that at least large-scale features of surface predictions in these areas are meaningful despite bed DEM error. Unfortunately bed data error is worse than 100 m over much of the GIS (Morlighem et al., 2014, 2015, 2017), making detailed surface predictions or inversions for parameters like basal sliding (C^*) unreliable in many regions with current data. We only use surface predictions from study regions R1 (shown in Fig. 7) and R2 in the following meltwater routing analysis.

3.2 Meltwater routing

3.2.1 Supraglacial stream network topographic conformity

We apply both stream network topographic conformity metrics as described in Section 2.4.3 to supraglacial stream networks from our seven study regions (Fig. 1.A, Table 1), and to synthetic flow networks from a non-fluvially-incised region and from two bed topography transfer predicted ice surfaces (in study regions R1 and R2). We find consistent trends in both $\%d$ (percent downhill) and Λ (conformity factor) for all stream and synthetic flow networks (Fig. 10). At the longest wavelength cutoffs $\%d$ and Λ are at their lowest values, and including shorter wavelengths generally results in increases in both metrics. $\%d$ and

The Cryosphere Discuss., https://doi.org/10.5194/tc-2018-74
Manuscript under review for journal The Cryosphere
Discussion started: 17 May 2018

Λ plateau at values between $88-97\%$ and $0.75-0.81$ respectively, except for in synthetic flow networks calculated on bed topography transfer predicted surfaces, where the metrics approach the expected maximum values of 100% and 1. The lower plateau values observed in real stream networks could be caused by varying channel depths and/or DEM inaccuracy.

Significantly, in all stream and synthetic flow networks, changes in both $\%d$ and Λ occur in bands of cutoff wavelengths roughly between 1 and 10 km. This indicates that these wavelengths of topography explain the general structure of supraglacial stream networks. These wavelength bands generally match the peaks in bed topography transfer predicted wavelengths (Fig. 9). In particular we note that the region where stream conformity is more affected by smaller wavelengths (solid red curves) would be expected to exhibit comparatively high bed topography transfer at these smaller wavelengths. The regions where stream conformity is less effected by smaller wavelengths (solid yellow, green, and purple curves) would be expected to exhibit comparatively low bed topography transfer at these wavelengths. This is consistent with empirical admittance calculations in Fig. 9.

3.2.2 Supraglacial stream network slope versus drainage area and thermal-fluvial incision

Individual supraglacial stream elevation profiles exhibit many readily visible deviations from idealized concave up longitudinal profiles (as described in Section 2.4.2) (Fig. 8). Supraglacial stream networks from our seven study areas (Fig. 1.A, Table 1) all exhibit negative slope versus drainage area relationships (thus positive concavity), as might be expected from fluvial control (Fig. 11). However, we also find negative slope-area trends in synthetic flow networks created by flow routing on an area of the GIS with no significant thermal-fluvial incision, and on two bed topography transfer predicted surfaces (from study regions R1 and R2). This is consistent with previous work showing that negative slope-area relations can arise even in randomly generated topography (Schorghofer and Rothman, 2002), making this often-used geomorphic metric challenging to invert uniquely for process.

Though the synthetic flow network slope-area trend from one supraglacial stream network (SN-R2) appears appreciably steeper than the corresponding synthetic flow network on a bed topography transfer predicted surface (FN-BTT-R2), overall the slope-area trends in synthetic flow networks appear to be similar to those on fluvially incised regions of the real ice surface, given the inherent scatter of slope-area relations (Warren et al., 2004). Further stream network data could allow for a finer distinguishment of slope-area relations between IDCs, but from these results it seems that bed topography transfer is sufficient to explain supraglacial stream longitudinal elevation profiles on at least $\sim$1-10 km scales, independent of thermal-fluvial incision.

4 Discussion

Our observations indicate that in regions of the GIS ablation zone with near-uniform ice velocity, given ice flow conditions (including basal sliding), bed topography transfer alone can explain $\sim$1-10 km scale ice sheet surface topography. Given moulin locations (which dictate where water leaves the surface environment), bed topography also explains both stream network

conformity metrics and stream network slope-area relations. We thus propose that bed topography transfer can explain the IDC-scale (∼1-10 km) structure of supraglacial meltwater routing.

4.1 Predicting supraglacial IDC evolution

Given moulin locations and ice flow conditions, bed topography transfer should generally explain IDC configurations, such as the trend observed by Yang and Smith (2016) where average IDC area increases with increasing ice surface elevation/thickness. It is expected that the ablation zone of the GIS will move to higher elevations in the coming years (Rae et al., 2012; Fettweis et al., 2013; Leeson et al., 2015). The method we have developed provides a tool to predict how the large scale structure of ice sheet surface drainage will respond to changes in ice flow and/or basal sliding, as might be expected to occur in the future. If moulin locations could also be predicted, this knowledge could then be used to predict the temporal input of surface meltwater into moulins with methods such as empirically calibrated hydrographs (e.g., Smith et al., 2017). Even without predicting moulin locations, we can still examine the general response of topographic basins to changing ice flow conditions.

The topographic basins associated with predicted ice surfaces under varying ice flow conditions are shown in Fig. 12. As discussed in Section 2.3.1, the timescale over which the ice sheet surface approaches 95% of its steady state configuration in response to a basal perturbation is on the order of 3-60 years depending upon perturbation wavelength (though some adjustment occurs much more rapidly), so our steady state predictions might be better interpreted as multi-year average ice surface configurations. If ice surface adjustments to variable basal conditions or ice flow perturbations are sufficiently rapid, surface topographic basin configuration should also vary on seasonal timescales.

We again note that topographic basins will not exactly correspond to IDCs (Smith et al., 2015; Yang et al., 2015; Yang and Smith, 2016). For comparison we show IDC configurations obtained solely from satellite imagery by Yang and Smith (2016) (Fig. 12). Despite the visible differences between our bed topography transfer predicted topographic basin configuration and the IDC configuration, the overall basin/IDC densities are similar. We thus expect that topographic basin density changes predicted with changing ice flow conditions should generally correspond to changes in IDC density. We find that changes in ice surface slope α or ice surface velocity U by factors of two do not significantly effect topographic basin density. However, we find that topographic basin density decreases appreciably with increasing ice thickness, and increases appreciably with increasing basal sliding. Our analysis thus indicates that ice surface topographic basin density in the GIS ablation zone could be significantly affected by perturbations to ice thickness or basal sliding.

4.2 Coupling between supraglacial IDC density and subglacial hydrologic regime

Basal sliding can change significantly on timescales as short as hours (Selmes et al., 2011; Sole et al., 2011; Chandler et al., 2013; Shannon et al., 2013), and is also the parameter that most significantly affects surface topographic basin density (Fig. 12). If average subglacial water pressure increases (due to less effective subglacial channelization) as moulin input becomes more disperse, this could lead to lower average basal effective stresses and thus increases in basal sliding (Werder et al., 2013; Banwell et al., 2016; Hoffman et al., 2018). The extent to which subglacial channelization occurs is debated (Meierbachtol et al., 2013), but some subglacial channelization may occur on timescales of hours to days with continuing evolution over the

The Cryosphere Discuss., https://doi.org/10.5194/tc-2018-74
Manuscript under review for journal The Cryosphere
Discussion started: 17 May 2018

length of melt seasons, and in the GIS ablation zone moulin meltwater input is a significant source of basal water effecting this subglacial drainage development (Schoof, 2010; Sole et al., 2011; Werder et al., 2013; Chandler et al., 2013).

Dispersing water input among more moulins could increase average basal water pressure (thus decreasing basal effective stress and increasing basal sliding) if water flux through each moulin becomes low enough to preclude efficient subglacial channel development. If this occurs, our results imply a positive feedback where increasing basal sliding increases IDC/moulin density which then further increases basal sliding. This feedback could be shut off by sufficiently decreased melt water production at the surface, by basin density increasing to the point that supraglacial lakes overflow to downslope catchments or do not rapidly build up water pressure for fracturing (Banwell et al., 2012, 2016), and/or by adjustment of other ice flow parameters to increased basal sliding (Hoffman and Price, 2014). Alternately, dispersing subglacial meltwater input among more moulins could result in more efficient subglacial drainage (thus lower basal water pressure and reduced sliding) if there is still sufficient water flux through each moulin to drive efficient subglacial channelization (Banwell et al., 2016). In this case there would be a negative feedback where increasing basal sliding increases IDC/moulin density, which then decreases basal sliding.

4.3 Thermal-fluvial incision on sub-IDC scales

Modeled melt rates in many areas of the GIS ablation zone are greater than 1 m/yr (water equivalent) (Noel et al., 2015), but the ice surface in these areas can be advecting stream channels horizontally across surface features from basal transfer at velocities greater than 100 m/yr (Joughin et al., 2010b, a; Nagler et al., 2015). Most IDCs on the GIS have maximum dimensions of 1-10s of km (Yang and Smith, 2016). Our admittance calculations indicate that bedrock transfer is less important for ice surface topography at scales $< \sim$1 km (Fig. 9), and we expect fluvial incision to be a more primary influence on meltwater routing pathways on these scales. On larger scales, our stream network and synthetic flow network analysis indicates that thermal-fluvial incision is convolved with bed topography controls on stream profiles (Fig. 11).

In terrestrial settings, bedrock fluvial incision is often modeled by the "stream power" law (Seidl and Dietrich, 1992). This semi-empirical model can be combined with Hack's law (Hack, 1957) relating downstream distance to accumulated flow area to predict surface lowering by mechanical erosion E of the substrate at point s along a stream channel downstream of a drainage divide at time t

$$E(s,t) = kA(s,t)^m \frac{\partial Z(s,t)}{\partial s}, \tag{7}$$

where A is accumulated drainage area, k is an experimentally determined coefficient, and m is an experimentally determined exponent.

In supraglacial environments fluvial erosion occurs by melting, but an analog of stream power may be derived (Karlstrom and Yang, 2016). Combined with a model for ice flow along the stream channel (Cuffey and Paterson, 2010), the following general surface evolution equation is obtained

$$\frac{\partial Z(s,t)}{\partial t} = -kA(s,t)^m \frac{\partial Z(s,t)}{\partial s} + f(s,t) \tag{8}$$

where f includes multiple terms that account for substrate movement (surface melting and ice flow) (Karlstrom and Yang, 2016).

In terrestrial settings, concave-up profiles and negative slope-area trends are often observed and interpreted as consequences of fluvial incision, because this is the steady state configuration approached by am erosionally controlled stream profile under uniform uplift (Gilbert, 1877; Whipple and Tucker, 1999; Montgomery, 2001). In the supraglacial environment, this concave-up configuration could be approached by streams with fixed terminal elevations such as supraglacial lakes (Karlstrom and Yang, 2016). Alternately, the erosion equation implies that for streams without fixed terminal elevations, such as those flowing over ice cliffs or into moulins, stream profiles should exhibit pervasive convexities due to transient changes at the boundary that persist through the time period of active incision (the melt season). Convexities induced by base level changes or non-uniform uplift propagate upstream as kinematic waves (Whipple and Tucker, 1999). In supraglacial streams, convexities could reflect such kinematic waves, transmitting impulsive uplift or erosion transients such as unsteady surface melting or supraglacial lake drainage (Hoffman et al., 2011). They might also record transient surface waves caused by ice flux variations (van de Wal and Oerlemans, 1995). Ice flux wave propagation speed likely differs from fluvial knickpoint propagation speed (Karlstrom and Yang, 2016).

In the terrestrial fluvial environment, convexities may also result from temporally steady but spatially variable uplift or substrate erodibility (Royden and Perron, 2013; OHara et al., submitted 2018). In the supraglacial environment, flow over rough bed topography, variable basal sliding or ice rheology, and/or deviations of the local ice velocity vector from the direction of stream flow (which could be caused by stream meanders, Karlstrom et al., 2013) could generate such convexities. If thermal-fluvial incision is slow enough relative to ice advection and/or other surface processes, stream profiles should not be significantly controlled by incision. In this case, channels would instead conform to the shape of the surrounding topography that is controlled by other processes.

Our conformity metric calculations (Fig. 10) are consistent with an external control on supraglacial stream network geometry. However, models that couple transient ice flow over rough bed topography to a surface energy balance will be necessary to rule out some influence of thermal-fluvial incision IDC-scale ice surface topography. Such models are also required to address observed supraglacial channel network coarsening (e.g., Yang and Smith, 2016), and to establish how diurnally and seasonally varying melt rates are imprinted on stream networks.

From the standpoint of predicting Greenland Ice Sheet-wide hydrology, our work may simplify future modeling efforts. If thermal-fluvial incision does not significantly modify the ice surface at IDC-scales, thermal-fluvial incision would not need to be fully coupled with ice sheet models in order account for meltwater routing and the general evolution of the ice surface. Rather, future work should focus on better predicting transfer of bed topography, basal sliding, and ice flux variations to the surface, and on predicting moulin formation. This work is needed to accurately predict the spatial distribution of IDCs through time.

5 Conclusions

Routing of GIS surface meltwater is important for understanding and predicting ice sheet evolution. To examine processes that control ablation zone surface topography and meltwater routing, we have implemented analytical 2D transfer functions

The Cryosphere Discuss., https://doi.org/10.5194/tc-2018-74
Manuscript under review for journal The Cryosphere
Discussion started: 17 May 2018

to predict the steady-state ice surface over rough bed topography and basal sliding variations, and applied them to multiple regions of the western GIS ablation zone with near-uniform ice surface velocity.

We find that bed topography transfer alone can reasonably well explain at least ∼1-10 km wavelength ice surface topography, and show that given moulin locations bed topography also explains the observed routing patterns of surface meltwater. We thus infer that bed topography is the dominant process controlling general IDC-scale (∼1-10 km) surface meltwater routing on the GIS ablation zone.

We demonstrate that bed topography transfer can be used to predict the general response of surface topographic basins to changing ice flow conditions in space or time. We propose a feedback by which the number density and size of IDCs are coupled to englacial input of meltwater that governs basal sliding efficacy.

Code and data availability. All codes and data produced by the authors available upon request. Ice surface DEMs are from SETSM ArcticDEM 2-10 m resolution mosaics (ArcticDEM, 2017). Bed DEMs are from Icebridge BedMachine (Morlighem et al., 2014, 2015). For ice surface velocity data is from MEaSUREs (Joughin et al., 2010b, a) and CCI SENTINEL-1 (Nagler et al., 2015). 2015 Melt data is from RACMO 2.3p2 (Noel et al., 2015).

Appendix A

A1 Time-Dependent Bed Topography and Basal Sliding Transfer Functions

We provide here a functional form of the ice surface transfer functions from Gudmundsson (2003) discussed in Section 2.3.1. We use the same notation as Gudmundsson (2003) except that we use k_U to denote wavenumber in the direction of ice velocity, and * to denote non-dimensionalized variables.

All parameters are non-dimensionalized prior to solving (noted with *). Ice surface velocity U is non-dimensionalized by the zeroth-order deformational velocity $U^* = U\frac{2\eta}{\rho g H^2 \sin(\alpha)}$. Basal sliding coefficient C is non-dimensionalized as $C^* = C\frac{2\eta}{H}$. Thus the non-dimensional zeroth-order (mean) basal sliding coefficient C^{0*} represents the ratio of zeroth-order basal sliding velocity to zeroth-order surface deformational velocity, or the mean slip ratio. All spatial variables including absolute wave-number k^* and wave-number in the direction of ice flow k_U^*, are non-dimensionalized by scaling to H. Time is non-dimensionalized as $t* = t\frac{\rho g H \sin(\alpha)}{2\eta}$.

The non-dimensionalized governing equations and boundary conditions are linearized around $\epsilon, \beta = 0$ and Fourier transformed (defined in Appendix A3). To obtain solutions the equations are Laplace transformed (as defined in Gudmundsson (2003)) in time. Solutions are in the form of transfer functions $\left(\hat{T}_B(k_x^*, k_y^*, t^*)\right.$ and $\left.\hat{T}_C(k_x^*, k_y^*, t^*)\right)$ for the ice surface response to bed topography and basal sliding perturbations, defined at time t^* from perturbations at time $t^* = 0$ to B^{0*} or C^{0*}. These transfer functions predict Z^* perturbations $\left(\text{where } Z^*(x^*, y^*, t) = Z^{1*}(x^*, y^*, t) + Z^{0*}(x^*, y^*)\right)$ in response to basal topography or sliding perturbations $\left(B^{1*}(x^*, y^*, 0) \text{ or } C^{1*}(x^*, y^*, 0)\right)$ as:

$$\hat{Z}^{1*}(k_x^*, k_y^*, t^*) = \hat{T}_B(k_x^*, k_y^*, t^*)\hat{B}^{1*}(k_x^*, k_y^*, 0) + \hat{T}_C(k_x^*, k_y^*, t^*)\hat{C}^{1*}(k_x^*, k_y^*, 0) \quad \text{(A1)}$$

The Cryosphere Discuss., https://doi.org/10.5194/tc-2018-74
Manuscript under review for journal The Cryosphere
Discussion started: 17 May 2018

Time-dependent bed topography transfer amplitude as a function of wave-number is

$$\hat{A}_B = ||\hat{T}_B|| = \frac{\tilde{a}}{\tilde{c}\sqrt{(\tilde{d}/\tilde{c})^2 + (\tilde{b}/\tilde{c})^2}} \sqrt{1 + e^{-t\tilde{b}/\tilde{c}}\left(e^{-t\tilde{b}/\tilde{c}} - 2\cos(t\tilde{d}/\tilde{c})\right)} \tag{A2}$$

and bed topography transfer phase shift ϕ (in radians) is

$$\hat{\phi}_B = \arctan\left(\frac{\mathbf{Im}(\hat{T}_B)}{\mathbf{Re}(\hat{T}_B)}\right) = \arctan\left(\frac{-\tilde{b} + e^{-t\tilde{b}/\tilde{c}}\left(\tilde{b}\cos(t\tilde{d}/\tilde{c}) - \tilde{d}\sin(t\tilde{d}/\tilde{c})\right)}{\tilde{d} - e^{-t\tilde{b}/\tilde{c}}\left(\tilde{d}\cos(t\tilde{d}/\tilde{c}) + \tilde{b}\sin(t\tilde{d}/\tilde{c})\right)}\right) \tag{A3}$$

and basal sliding transfer amplitude is

$$\hat{A}_C = ||\hat{T}_C|| = \frac{-\tilde{g}}{\tilde{c}\sqrt{(\tilde{d}/\tilde{c})^2 + (\tilde{b}/\tilde{c})^2}} \sqrt{1 + e^{-t\tilde{b}/\tilde{c}}\left(e^{-t\tilde{b}/\tilde{c}} - 2\cos(t\tilde{d}/\tilde{c})\right)} \tag{A4}$$

and basal sliding transfer phase shift ϕ_C (in radians) is

$$\hat{\phi}_C = \arctan\left(\frac{\mathbf{Im}(\hat{T}_C)}{\mathbf{Re}(\hat{T}_C)}\right) = \phi_B + \pi \tag{A5}$$

where

$$\tilde{a} = \left(U^*\tilde{f} + (U^* + k^{*2}C^{*(2)})\cosh(k^*)\right)k^*k_U^*$$

$$\tilde{b} = (\tilde{f}\sinh(k^*) - k^*)\cot(\alpha)$$

$$\tilde{c} = k^{*(3)}U^* + \tilde{f}k^*\cosh(k^*)$$

$$\tilde{d} = k_U^*U^*(\tilde{c} + k^*)$$

$$\tilde{g} = -k_U^*k^*C^*\cosh(k^*)$$

$$\tilde{f} = \cosh(k^*) + k^*C^*\sinh(k^*).$$

The ice surface perturbation propagation timescale (the time over which surface perturbations are advected down-flow by one wavelength) is given by:

$$t_p^* = \tilde{c}/\tilde{b} \tag{A6}$$

and the ice surface perturbation decay timescale (the timescale governing surface rise/depression rate from a basal perturbation) is given by:

$$t_d^* = \tilde{c}/\tilde{d}. \tag{A7}$$

A2 Transfer Function Dependence on 2D Bed Topography

We use the bed topography transfer functions from Gudmundsson (2003) (and defined in Appendix A1) to demonstrate that predicted bed topography transfer amplitude and phase depend upon the angle θ of bed topographic features relative to the ice

The Cryosphere Discuss., https://doi.org/10.5194/tc-2018-74
Manuscript under review for journal The Cryosphere
Discussion started: 17 May 2018

flow direction, as described in Section 2.3.2. By setting $k^* = k_U^* \cos(\theta)$ for a range of θ $\left(\theta \neq \frac{n\pi}{2}\right)$, it can be shown that bed topography transfer amplitude depends upon θ as

$$\hat{A}_B(\theta) = \left(k_U^{*(2)} \cos(\theta) \left(\cosh(k_U^* \cos(\theta)) \left(C^{0*(2)} k_U^{*(2)} \cos^2(\theta) + 2U^* \right) + C^{0*} k_U^* U^* \cos(\theta) \sinh(k_U^* \cos(\theta)) \right) \right) / \ldots$$
$$\left(k_U^{*(4)} U^{*(2)} \cos^2(\theta) \left(\frac{1}{2} C^{0*} k_U^* \cos(\theta) \sinh(2k_U^* \cos(\theta)) + k_U^{*(2)} U^* \cos^2(\theta) + \cosh^2(k_U^* \cos(\theta)) + 1 \right)^2 + \ldots \right.$$
$$\left. \cot^2(\alpha) \left(k_U^* \cos(\theta) \left(C^{0*} \sinh^2(k_U^* \cos(\theta)) - 1 \right) + \frac{1}{2} \sinh(2k_U^* \cos(\theta)) \right)^2 \right)^{1/2}. \quad \text{(A8)}$$

It can similarly be shown that bed topography transfer phase also depends upon θ as

$$\hat{\phi}_B(\theta) = -\text{arccot} \left(\frac{k_U^{*(2)} v \tan(\alpha) \cos(\theta) \left(C^{0*} k_U^* \cos(\theta) \sinh(2k_U^* \cos(\theta)) + 2k_U^{*(2)} v \cos^2(\theta) + \cosh(2k_U^* \cos(\theta)) + 3 \right)}{2k_U^* \cos(\theta) \left(C^{0*} \sinh^2(k_U^* \cos(\theta)) - 1 \right) + \sinh(2k_U^* \cos(\theta))} \right). \quad \text{(A9)}$$

These equations give the potential variation in bed topography transfer amplitude and phase that could result from examining bed topography only along ice flowline transects, and thus demonstrate the importance of predicting the ice surface over 2D bed topography.

A3 Fourier Transform

Fourier transforms are used in the derivation of the bed topography and basal sliding transfer functions. Via the convention of Gudmundsson (2003), the Fourier transform $\mathcal{F}$ of a continuous function $f(x, y)$ is defined as

$$\mathcal{F}(f(x,y)) = \hat{f}(k_x, k_y) = \int_{-\infty}^{\infty} \int_{-\infty}^{\infty} f(x,y) e^{i(k_x x + k_y y)} dx dy, \quad \text{(A10)}$$

where k_x, k_y are wavenumbers in the x and y directions and $i = \sqrt{-1}$. The inverse Fourier transform is then

$$\mathcal{F}^{-1}(\hat{f}(k_x, k_y)) = f(x,y) = \frac{1}{4\pi^2} \int_{-\infty}^{\infty} \int_{-\infty}^{\infty} f(k_x, k_y) e^{-i(k_x x + k_y y)} dk_x dk_y. \quad \text{(A11)}$$

We use DFTs and inverse DFTs for both data processing and basal transfer function implementation, we calculate these on 1D and 2D data using Matlab version R2017b.

A4 Conformity Metrics

We use two conformity metrics, $\%d$ and Λ, to examine how well stream network geometry is explained by surface topography lowpass filtered at various wavelengths as described in Section 2.4.3. We project stream networks onto filtered surfaces and

The Cryosphere Discuss., https://doi.org/10.5194/tc-2018-74
Manuscript under review for journal The Cryosphere
Discussion started: 17 May 2018

then for each stream we calculate conformity factor as:

$$\Lambda = \frac{1}{L} \int_{l=1}^{L} \left| \frac{\boldsymbol{D}(l) \bullet (\boldsymbol{\nabla} Z(l))}{\|\boldsymbol{D}(l)\| \|\boldsymbol{\nabla} Z(l)\|} \right| dl \tag{A12}$$

where $\|\|$ indicates vector magnitude, $\boldsymbol{D}(l) = (D_x(l), D_y(l))$ is the stream channel horizontal direction vector (the east-north direction of water flow, calculated with a 2nd order centered difference approximation of the stream channel tangent in map-view) at location l along a stream of length L, and $\boldsymbol{\nabla} Z(l)$ is the corresponding ice surface gradient $\left(\frac{\partial Z}{\partial x}|_l, \frac{\partial Z}{\partial y}|_l\right)$ (calculated with a 2nd order centered difference approximation). We calculate percent downhill (here using discrete notation) as:

$$\%d = \frac{100}{N-1} \sum_{n=1}^{N-1} \begin{cases} 0 & \text{if } Z(n) \leq Z(n+1) \\ 1 & \text{if } Z(n) > Z(n+1) \end{cases} \tag{A13}$$

where n indexes discrete location along a stream (n increases in the downstream direction), $Z(n)$ is the corresponding ice surface elevation, and N is the number of discrete locations along the stream, where each location corresponds to a DEM pixel. To calculate $\%d$ and Λ for a whole stream network we calculate $\%d$ and Λ for each stream segment in the network, then take a weighted average of each metric over all stream segments, where data from each stream segment is weighted by the number of data points in that segment (N).

Competing interests. No competing interests are present.

Acknowledgements. We thank Colin Meyer, Dan O'Hara, and Alan Rempel for their input and discussions. LK acknowledges funding from NASA award NNX16AQ56G

References

Andersen, M. L., Stenseng, L., Skourup, H., Colgan, W., Khan, S. A., Kristensen, S. S., Andersen, S. B., Box, J. E., Ahlstrøm, A. P., Fettweis, X., and Forsbergb, R.: Basin-scale partitioning of Greenland ice sheet mass balance components (2007–2011), Earth and Planetary Science Letters, 409, 89–95, https://doi.org/10.1016/j.epsl.2014.10.015, 2015.

ArcticDEM: DEMs provided by the Polar Geospatial Center under NSF OPP awards 1043681, 1559691 and 1542736, 2017.

Banwell, A., Hewitt, I., Willis, I., and Arnold, N.: Moulin density controls drainage development beneath the Greenland ice sheet, Journal of Geophysical Research: Earth Surface, 121, 2248–2269, https://doi.org/10.1002/2015JF003801, 2016.

Banwell, A. F., Arnold, N. S., Willis, I. C., Tedesco, M., and Ahlstrøm, A. P.: Modeling supraglacial water routing and lake filling on the Greenland Ice Sheet, Journal of Geophysical Research: Earth Surface, 117, https://doi.org/10.1029/2012JF002393, 2012.

Bartholomew, I. D., Nienow, P., Sole, A., Mair, D., Cowton, T., King, M. A., and Palmer, S.: Seasonal variations in Greenland Ice Sheet motion: Inland extent and behaviour at higher elevations, Earth and Planetary Science Letters, 307, 271–278, 2011.

Black, B. A., Perron, T. J., Hemingway, D., Bailey, E., Nimmo, F., and Zebker, H.: Global drainage patterns and the origins of topographic relief on Earth, Mars, and Titan, Science, 356, 727–731, https://doi.org/10.1126/science.aag0171, 2017.

Boisvert, L. N., Lee, J. N., Lenaerts, J. T. M., Noël, B., van den Broeke, M. R., and Nolin, A. W.: Using remotely sensed data from AIRS to estimate the vapor flux on the Greenland ice sheet: Comparisons with observations and a regional climate model, Journal of Geophysical Research:Atmosphere, 122, 202–229, https://doi.org/10.1002/2016JD025674, 2017.

Catania, G. A., Neumann, T. A., and Price, S. F.: Characterizing englacial drainage in the ablation zone of the Greenland ice sheet, Journal of Glaciology, 54, 567–578, https://doi.org/10.3189/002214308786570854, 2008.

Chandler, D. M., Wadham, J. L., Lis, G. P., Cowton, T., Sole, A., Bartholomew, I., Telling, J., Nienow, P., Bagshaw, E. B., Mair, D., Vinen, S., and Hubbard, A.: Evolution of the subglacial drainage system beneath the Greenland Ice Sheet revealed by tracers, Nature Geoscience, 6, 195–198, https://doi.org/10.1038/ngeo1737, 2013.

Chu, V. W.: Greenland ice sheet hydrology: A review, Progress in Physical Geography: Earth and Environment, 38, 19–54, https://doi.org/10.1177/0309133313507075, 2014.

Cuffey, K. M. and Paterson, W. S. B.: The Physics of Glaciers, Academic Press, 4 edn., 2010.

Das, S. B., Joughin, I., Behn, M. D., Howat, I. M., King, M. A., Lizarralde, D., and Bhatia, M. P.: Fracture Propagation to the Base of the Greenland Ice Sheet During Supraglacial Lake Drainage, Science, 320, 778–781, https://doi.org/10.1126/science.1153360, 2008.

De Rydt, J., Gudmundsson, G. H., Corr, H. F. J., and Christoffersen, P.: Surface undulations of Antarctic ice streams tightly controlled by bedrock topography, The Cryosphere, 7, 407–417, https://doi.org/10.5194/tc-7-407-2013, https://www.the-cryosphere.net/7/407/2013/, 2013.

Echelmeyer, K., Clarke, T. S., and Harrison, W. D.: Surficial glaciology of Jakobshavns Isbræ, West Greenland: Part I. Surface morphology, Journal of Glaciology, 37, 368–382, https://doi.org/10.3189/S0022143000005803, 1991.

Enderlin, E. M., Howat, I. M., Jeong, S., Noh, M.-J., van Angelen, J. H., and van den Broeke, M. R.: An improved mass budget for the Greenland ice sheet, Geophysical Research Letters, 41, 866–872, https://doi.org/10.1002/2013GL059010, http://dx.doi.org/10.1002/2013GL059010, 2013GL059010, 2014.

Fettweis, X., Franco, B., Tedesco, M., van Angelen, J. H., Lenaerts, J. T. M., van den Broeke, M. R., and Gallée, H.: Estimating the Greenland ice sheet surface mass balance contribution to future sea level rise using the regional atmospheric climate model MAR, The Cryosphere, 7, 469–489, https://doi.org/10.5194/tc-7-469-2013, https://www.the-cryosphere.net/7/469/2013/, 2013.

Fountain, A. G. and Walder, J. S.: Water flow through temperate glaciers, Reviews of Geophysics, 36, 299–328, https://doi.org/10.1029/97RG03579, http://dx.doi.org/10.1029/97RG03579, 1998.

Fowler, A. C.: Restricted access A sliding law for glaciers of constant viscosity in the presence of subglacial cavitation, Procedings of the Royal Society, 407, 147–170, https://doi.org/10.1098/rspa.1986.0090, 1986.

Gagliardini, O., Zwinger, T., Gillet-Chaulet, F., Durand, G., Favier, L., de Fleurian, B., Greve, R., Malinen, M., Martín, C., Råback, P., Ruokolainen, J., Sacchettini, M., Schäfer, M., Seddik, H., and Thies, J.: Capabilities and performance of Elmer/Ice, a new-generation ice sheet model, Geoscientific Model Development, 6, 1299–1318, https://doi.org/10.5194/gmd-6-1299-2013, https://www.geosci-model-dev.net/6/1299/2013/, 2013.

Gilbert, G. K.: Geology of the Henry Mountains, U.S Geographical and Geological Survey of the Rocky Mountain Region, 1877.

Gillet-Chaulet, F., Gagliardini, O., Seddik, H., Nodet, M., Durand, G., Ritz, C., Zwinger, T., Greve, R., and Vaughan, D. G.: Greenland ice sheet contribution to sea-level rise from a new-generation ice-sheet model, The Cryosphere, 6, 1561–1576, https://doi.org/10.5194/tc-6-1561-2012, https://www.the-cryosphere.net/6/1561/2012/, 2012.

Graham, F. S., Morlighem, M., Warner, R. C., and Treverrow, A.: Implementing an empirical scalar tertiary anisotropic rheology (ESTAR) into large-scale ice sheet models, The Cryosphere Discuss, https://doi.org/10.5194/tc-2017-54, 2017.

Gudmundsson, G. H.: Transmission of basal variability to a glacier surface, Journal of Geophysical Research, 108, https://doi.org/10.1029/2002JB002107, 2003.

Hack, J. T.: Studies of longitudinal stream profiles in Virginia and Maryland, USGS Professional Papers, 294-B, 1957.

Hart, J. K.: Subglacial erosion, deposition and deformation associated with deformable beds, Progress in Physical Geography: Earth and Environment, 19, 173–191, https://doi.org/10.1177/030913339501900202, 1995.

Helm, V., Humbert, A., and Miller, H.: Elevation and elevation change of Greenland and Antarctica derived from CryoSat-2, The Cryosphere, 8, 1539–1559, https://doi.org/10.5194/tc-8-1539-2014, 2014.

Hewitt, I. J. and Fowler, A. C.: Seasonal waves on glaciers, Hydrological Processes, 22, 3919–3930, https://doi.org/10.1002/hyp.7029, 2008.

Hoffman, M. and Price, S.: Feedbacks between coupled subglacial hydrology and glacier dynamics, Journal of Geophysical Research: Earth Surface, 119, 414–436, https://doi.org/10.1002/2013JF002943, 2014.

Hoffman, M. J., Catania, G. A., Neumann, T. A., Andrews, L. C., and Rumrill, J. A.: Links between acceleration, melting, and supraglacial lake drainage of the western Greenland Ice Sheet, Journal of Geophysical Research: Earth Surface, 116, https://doi.org/10.1029/2010JF001934, 2011.

Hoffman, M. J., Perego, M., Andrews, L. C., Price, S. F., Neumann, T. A., Johnson, J. V., Catania, G., and Lüthi, M. P.: Widespread Moulin Formation During Supraglacial Lake Drainages in Greenland, Geophysical Research Letters, 45, 778–788, https://doi.org/10.1002/2017GL075659, 2018.

Huybrechts, P.: Basal temperature conditions of the Greenland ice sheet during the glacial cycles, Annals of Glaciology, 23, 226–236, https://doi.org/10.3189/S0260305500013483, 1996.

Joughin, I., Smith, B., Howat, I., and Scambos, T.: MEaSUREs Greenland Ice Velocity Map from InSAR Data, National Snow and Ice Data Center, https://doi.org/10.5067/MEASURES/CRYOSPHERE/nsidc-0478.001, 2010a.

Joughin, I., Smith, B., Howat, I. M., Scambos, T., and Moon, T.: Greenland Flow Variability from Ice-Sheet-Wide Velocity Mapping, Journal of Glaciology, 56, 415–430, https://doi.org/10.3189/002214310792447734, 2010b.

Karlstrom, L. and Yang, K.: Fluvial supraglacial landscape evolution on the Greenland Ice Sheet, Geophysical Research Letters, 43, 2683–2692, https://doi.org/10.1002/2016GL067697, 2016.

Karlstrom, L., Gajjar, P., and Manga, M.: Meander formation in supraglacial streams, Journal of Geophysical Research Earth Surface, 118, 1897–1907, https://doi.org/10.1002/jgrf.20135, 2013.

Khan, S. A., Aschwanden, A., Bjørk, A. A., Wahr, J., Kjeldsen, K. K., and Kjær, K. H.: Greenland ice sheet mass balance: a review, IOP Reports on Progress in Physics, https://doi.org/https://doi.org/10.1088/0034-4885/78/4/046801, 2015.

Koenig, L. S., Ivanoff, A., Alexander, P. M., MacGregor, J. A., Fettweis, X., Panzer, B., Paden, J. D., Forster, R. R., Das, I., McConnell, J. R., Tedesco, M., Leuschen, C., and Gogineni, P.: Annual Greenland accumulation rates (2009–2012) from airborne snow radar, The Cryosphere, 10, 1739–1752, https://doi.org/10.5194/tc-10-1739-2016, https://www.the-cryosphere.net/10/1739/2016/, 2016.

Lampkin, D. J.: Supraglacial lake spatial structure in western Greenland during the 2007 ablation season, Journal of Geophysical Research: Earth Surface, 116, n/a–n/a, https://doi.org/10.1029/2010JF001725, http://dx.doi.org/10.1029/2010JF001725, f04001, 2011.

Lampkin, D. J. and van der Berg, J.: A preliminary investigation of the influence of basal and surface topography on supraglacial lake distribution near Jakobshavn Isbrae, western Greenland, Hydrological Processes, 25, 3347–3355, https://doi.org/10.1002/hyp.8170, 2011.

Larour, E., Seroussi, H., Morlighem, M., and Rignot, E.: Continental scale, high order, high spatial resolution, ice sheet modeling using the Ice Sheet System Model (ISSM), Journal of Geophysical Research: Earth Surface, 117, https://doi.org/10.1029/2011JF002140, 2012.

Leeson, A. A., Shepherd, A., Briggs, K., Howat, I., Fettweis, X., Morlighem, M., and Rignot, E.: Supraglacial lakes on the Greenland ice sheet advance inland under warming climate, Nature Climate Change, 5, 51–55, https://doi.org/10.1038/nclimate2463, 2015.

Lipscomb, W. H., Fyke, J. G., Vizcaíno, M., Sacks, W. J., Wolfe, J., Vertenstein, M., Craig, A., Kluzek, E., and Lawrence, D. M.: Implementation and Initial Evaluation of the Glimmer Community Ice Sheet Model in the Community Earth System Model, Journal of Climate, 26, 7352–7371, https://doi.org/10.1175/JCLI-D-12-00557.1, 2013.

MacGregor, J. A., Fahnestock, M. A., Catania, G. A., Aschwanden, A., Clow, G. D., Colgan, W. T., Gogineni, S. P., Morlighem, M., Nowicki, S. M. J., Paden, J. D., Price, S. F., and Seroussi, H.: A synthesis of the basal thermal state of the Greenland Ice Sheet, Journal of Geophysical Research: Earth Surface, 121, 1328–1350, https://doi.org/10.1002/2015JF003803, 2016.

Mackey, B. H. and Roering, J. J.: Sediment yield, spatial characteristics, and the long-term evolution of active earthflows determined from airborne LiDAR and historical aerial photographs, Eel River, California, GSA Bulletin, 123, 1560–1576, https://doi.org/10.1130/B30306.1, 2011.

Meierbachtol, T., Harper, J., and Humphrey, N.: Basal Drainage System Response to Increasing Surface Melt on the Greenland Ice Sheet, Science, 341, 777–779, https://doi.org/10.1126/science.1235905, 2013.

Meyer, C. R. and Hewitt, I. J.: A continuum model for meltwater flow through compacting snow, The Cryosphere, 11, 2799–2813, https://doi.org/10.5194/tc-11-2799-2017, https://www.the-cryosphere.net/11/2799/2017/, 2017.

Montgomery, D.: Slope Distributions, Threshold Hillslopes, and Steady-state Topography, American Journal of Science, 301, 432–454, https://doi.org/10.2475/ajs.301.4-5.432, 2001.

Morlighem, M., Seroussi, H., Larour, E., and Rignot, E.: Inversion of basal friction in Antarctica using exact and incomplete adjoints of a higher-order model, Journal of Geophysical Research: Earth Surface, 118, 1746–1753, https://doi.org/10.1002/jgrf.20125, 2013.

Morlighem, M., Rignot, E., Mouginot, J., Seroussi, H., and Larour, E.: Deeply incised submarine glacial valleys beneath the Greenland Ice Sheet, Nature Geoscience, 7, 418–422, https://doi.org/10.1038/ngeo2167, 2014.

Morlighem, M., Rignot, E., Mouginot, J., Seroussi, H., and Larour, E.: IceBridge BedMachine Greenland, Version 2, NASA DAAC at the National Snow and Ice Data Center, https://doi.org/10.5067/AD7B0HQNSJ29, 2015.

Morlighem, M., Williams, C. N., Rignot, E., An, L., Arndt, J. E., Bamber, J. L., Catania, G., Chauché, N., Dowdeswell, J. A., Dorschel, B., Fenty, I., Hogan, K., Howat, I., Hubbard, A., Jakobsson, M., Jordan, T. M., Kjeldsen, K. K., Millan, R., Mayer, L., Mouginot, J., Noël, B. P. Y., O'Cofaigh, C., Palmer, S., Rysgaard, S., Seroussi, H., Siegert, M. J., Slabon, P., Straneo, F., van den Broeke, M. R., Weinrebe, W., Wood, M., and Zinglersen, K. B.: BedMachine v3: Complete Bed Topography and Ocean Bathymetry Mapping of Greenland From Multibeam Echo Sounding Combined With Mass Conservation, Geophysical Research Letters, 44, 11,051–11,061, https://doi.org/10.1002/2017GL074954, 2017.

Nagler, T., Rott, H., Hetzenecker, M., Wuite, J., and Potin, P.: The Sentinel-1 Mission: New Opportunities for Ice Sheet Observations, Remote Sensing, 7, 9371–9389, https://doi.org/10.3390/rs70709371, 2015.

Noel, B., van de Berg, W. J., van Meijgaard, E., Munneke, P. K., van de Wal, R. S. W., and van den Broeke, M. R.: Evaluation of the updated regional climate model RACMO2.3: summer snowfall impact on the Greenland Ice Sheet, The Cryosphere, 9, 1831–1844, https://doi.org/doi:10.5194/tc-9-1831-2015, 2015.

Noh, M.-J. and Howat, I. M.: Automated stereo-photogrammetric DEM generation at high latitudes: Surface Extraction with TIN-based Search-space Minimization (SETSM) validation and demonstration over glaciated regions, GIScience and Remote Sensing, 52, 198–217, https://doi.org/10.1080/15481603.2015.1008621, 2015.

Nye, J. F.: The response of glaciers and ice-sheets to seasonal and climatic changes, Proc. Royal Society, 256, 559–584, https://doi.org/10.1098/rspa.1960.0127, 1960.

OHara, D., Karlstrom, L., and Roering, J. J.: Distributed landscape response to localized uplift and the fragility of steady states, Submitted to Elsevier, submitted 2018.

Parker, G.: Meandering of supraglacial melt streams, Water Resources Research, 11, 551–552, 1975.

Perron, J. T., Kirchner, J. W., and Dietrich, W. E.: Spectral signatures of characteristic spatial scales and nonfractal structure in landscapes, Journal of Geophysical Research, 113, https://doi.org/10.1029/2007JF000866, 2008.

Rae, J. G. L., AÃ°algeirsdóttir, G., Edwards, T. L., Fettweis, X., Gregory, J. M., Hewitt, H. T., Lowe, J. A., Lucas-Picher, P., Mottram, R. H., Payne, A. J., Ridley, J. K., Shannon, S. R., van de Berg, W. J., van de Wal, R. S. W., and van den Broeke, M. R.: Greenland ice sheet surface mass balance: evaluating simulations and making projections with regional climate models, The Cryosphere, 6, 1275–1294, https://doi.org/10.5194/tc-6-1275-2012, https://www.the-cryosphere.net/6/1275/2012/, 2012.

Raymond, M. J. and Gudmundsson, G. H.: Estimating basal properties of ice streams from surface measurements: a non-linear Bayesian inverse approach applied to synthetic data, The Cryosphere, 3, 265–278, https://doi.org/10.5194/tc-3-265-2009, 2009.

Royden, L. and Perron, J. T.: Solutions of the stream power equation and application to the evolution of river longitudinal profiles, Journal of Geophysical Research Earth Surface, 118, 497–518, https://doi.org/10.1002/jgrf.20031, 2013.

Schoof, C.: Ice-sheet acceleration driven by melt supply variability, Nature, 468, 803–806, https://doi.org/10.1038/nature09618, 2010.

Schorghofer, N. and Rothman, D. H.: Acausal relations between topographic slope and drainage area, Geophysical Research Letters, 29, 11–1–11–4, https://doi.org/10.1029/2002GL015144, http://dx.doi.org/10.1029/2002GL015144, 2002.

Schwanghart, W, S. D.: TopoToolbox 2 – MATLAB-based software for topographic analysis and modeling in Earth surface sciences, Earth Surface Dynamics, 2, 1–7, https://doi.org/10.5194/esurf-2-1-2014, 2014.

Seidl, M. A. and Dietrich, W. E.: The problem of channel erosion into bedrock, Catena Supplement, 23, 101–124, 1992.

Selmes, N., Murray, T., and James, T. D.: Fast draining lakes on the Greenland Ice Sheet, Geophysical Research Letters, 38, n/a–n/a, https://doi.org/10.1029/2011GL047872, http://dx.doi.org/10.1029/2011GL047872, l15501, 2011.

Sergienko, O. V.: Glaciological twins: basally controlled subglacial and supraglacial lakes, Journal of Glaciology, 59, 3–8, https://doi.org/10.3189/2013JoG12J040, 2013.

Shannon, S. R., Payne, A. J., Bartholomew, I. D., van den Broeke, M. R., Edwards, T. L., Fettwei, X., Gagliardini, O., Gillet-Chaulet, F., Goelzer, H., Hoffman, M. J., Huybrechts, P., Mair, D. W. F., Nienow, P. W., Perego, M., Price, S. F., Smeets, C. J. P. P., Sole, A. J., van de Wal, R. S. W., and Zwinger, T.: Enhanced basal lubrication and the contribution of the Greenland ice sheet to future sea-level rise, Proceedings of the National Academy of Sciences, 110, 14 156–14 161, https://doi.org/10.1073/pnas.1212647110, 2013.

Smith, L., Yang, K., Pitcher, L., Overstreet, B., Chu, V., Rennermalm, A., Ryan, J., Cooper, M., Gleason, C., Tedesco, M., Jeyeratnam, J., As, D., Broeke, M., Berg, W., Noel, B., Langen, P., Cullather, R., Zhao, B., Willis, M., Hubbard, A., Box, J., Jenner, B., and Behar, A.: Direct measurements of meltwater runoff on the Greenland ice sheet surface, Proceedings of the National Academy of Sciences, https://doi.org/10.1073/pnas.1707743114, 2017.

Smith, L. C., Chu, V. W., Yang, K., Gleason, C. J., Pitcher, L. H., Rennermalm, A. K., Legleiter, C. J., Behar, A. E., Overstreet, B. T., Moustafa, S. E., Tedesco, M., Forster, R. R., LeWinter, A. L., Finnegan, D. C., Sheng, Y., and Balog, J.: Efficient meltwater drainage through supraglacial streams and rivers on the southwest Greenland ice sheet, Proceedings of the National Academy of Sciences, 112, 1001–1006, https://doi.org/10.1073/pnas.1413024112, 2015.

Sole, A. J., Mair, D. W. F., Nienow, P. W., Bartholomew, I. D., King, M. A., Burke, M. J., and Joughin, I.: Seasonal speedup of a Greenland marine-terminating outlet glacier forced by surface melt–induced changes in subglacial hydrology, Journal of Geophysical Research: Earth Surface, 116, https://doi.org/10.1029/2010JF001948, http://dx.doi.org/10.1029/2010JF001948, 2011.

Stein, S. and Wysession, M.: An Introduction to Seismology, Earthquakes, and Earth Structure, Blackwell Publishing, 2005.

Stevens, L. A., Behn, M. D., McGuire, J. J., Das, S. B., Joughin, I., Herring, T., Shean, D. E., and King, M. A.: Greenland supraglacial lake drainages triggered by hydrologically induced basal slip, Nature, 522, 73–76, https://doi.org/10.1038/nature14480, 2015.

Sugden, D. E.: Glacial Erosion by the Laurentide Ice Sheet, Journal of Glaciology, 20, 367–391, https://doi.org/10.3189/S0022143000013915, 1978.

Tulaczyk, S., Kamb, W. B., and Engelhardt, H. F.: Basal mechanics of Ice Stream B, west Antarctica: 2 Undrained plastic bed model, Journal of Geophysical Research: Solid Earth, 105, 483–494, https://doi.org/10.1029/1999JB900328, http://dx.doi.org/10.1029/1999JB900328, 2000.

van de Wal, R. S. W. and Oerlemans, J.: Response of valley glaciers to climate change and kinematic waves: A study with a numerical ice-flow model, Journal of Glaciology, 41, 142–152, 1995.

van den Broeke, M., Bamber, J., Ettema, J., Rignot, E., Schrama, E., van de Berg, W. J., van Meijgaard, E., Velicogna, I., and Wouters, B.: Partitioning Recent Greenland Mass Loss, Science, 326, 984–986, https://doi.org/10.1126/science.1178176, 2009.

van den Broeke, M. R., Smeets, C. J. P. P., and van de Wal, R. S. W.: The seasonal cycle and interannual variability of surface energy balance and melt in the ablation zone of the west Greenland ice sheet, The Cryosphere, 5, 377–390, https://doi.org/10.5194/tc-5-377-2011, https://www.the-cryosphere.net/5/377/2011/, 2011.

Warren, S. D., Hohmann, M. G., Auerswald, K., and Mitasova, H.: An evaluation of methods to determine slope using digital elevation data, CATENA, 58, 215–233, https://doi.org/10.1016/j.catena.2004.05.001, 2004.

Weertman, J.: Traveling waves on glaciers, Physics of the Movement of Ice, 1958.

Wegmann, K. W., Zurek, B. D., Regalla, C. A., Bilardello, D., Wollenberg, J. L., Kopczynski, S. E., Ziemann, J. M., Haight, S. L., Apgar, J. D., Zhao, C., and Pazzaglia, F. J.: Position of the Snake River watershed divide as an indicator of geodynamic processes in the greater Yellowstone region, western North America, Geosphere, 3, 271–281, https://doi.org/10.1130/GES00083.1, 2007.

Werder, M. A., Hewitt, I. J., Schoof, C. G., and Flowers, G. E.: Modeling channelized and distributed subglacial drainage in two dimensions, Journal of Geophysical Research: Earth Surface, 118, 2140–2158, https://doi.org/10.1002/jgrf.20146, http://dx.doi.org/10.1002/jgrf.20146, 2013.

Whipple, K. X. and Tucker, G. E.: Dynamics of the stream-power river incision model: Implications for height limits of mountain ranges, landscape response timescales, and research needs, Journal of Geophysical Research: Solid Earth, 104, 17 661–17 674, https://doi.org/10.1029/1999JB900120, http://dx.doi.org/10.1029/1999JB900120, 1999.

Yang, K. and Smith, L. C.: Internally drained catchments dominate supraglacial hydrology of the southwest Greenland Ice Sheet, Journal of Geophysical Research: Earth Surface, 121, https://doi.org/10.1002/2016JF003927, 2016.

Yang, K., Smith, L. C., Chu, V. W., Gleason, C. J., and Li, M.: A Caution on the Use of Surface Digital Elevation Models to Simulate Supraglacial Hydrology of the Greenland Ice Sheet, IEEE Journal of Selected Topics in Applied Earth Observations and Remote Sensing, 8, 5212–5224, https://doi.org/10.1109/JSTARS.2015.2483483, 2015.

Zwally, H. J., Abdalati, W., Herring, T., Larson, K., Saba, J., and Steffen, K.: Surface Melt-Induced Acceleration of Greenland Ice-Sheet Flow, Science, 297, 218–222, https://doi.org/10.1126/science.1072708, 2002.

Ádám Ignéczi, Sole, A. J., Livingstone, S. J., Leeson, A. A., Fettweis, X., Selmes, N., Gourmelen, N., and Briggs, K.: Northeast sector of the Greenland Ice Sheet to undergo the greatest inland expansion of supraglacial lakes during the 21st century, Geophysical Research Letters, 43, 9729–9738, https://doi.org/10.1002/2016GL070338, 2016.

The Cryosphere Discuss., https://doi.org/10.5194/tc-2018-74
Manuscript under review for journal The Cryosphere
Discussion started: 17 May 2018

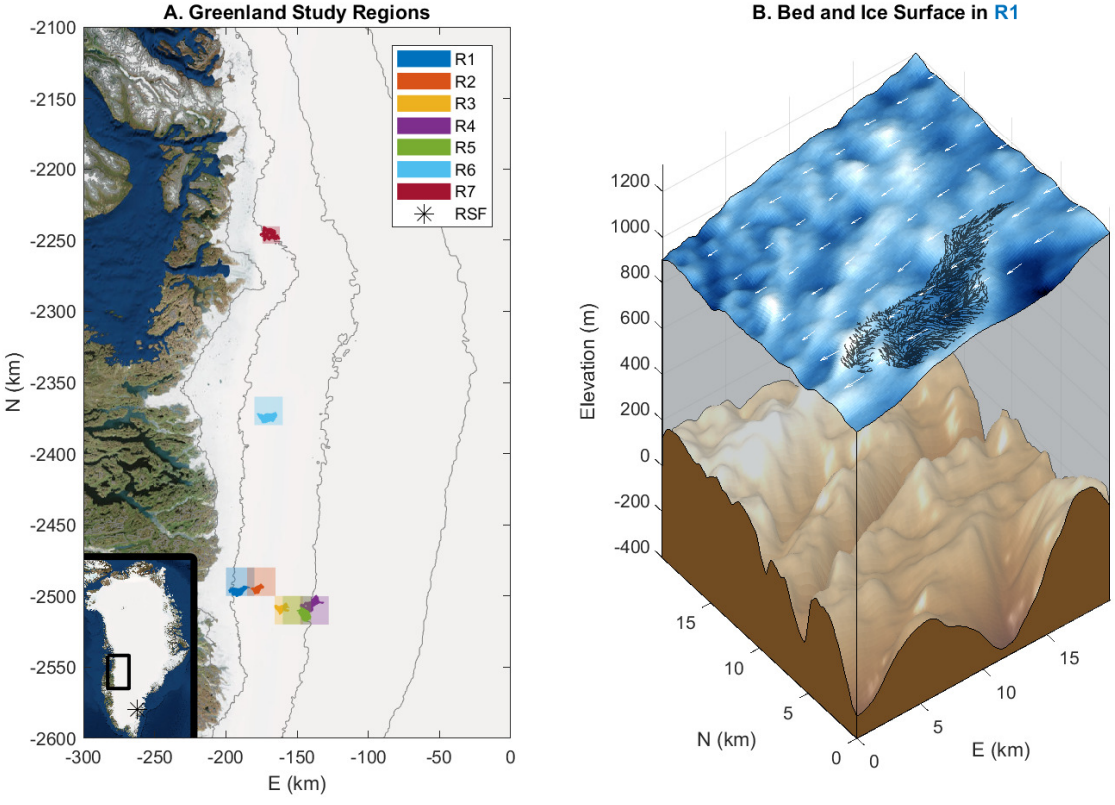

Figure 1. (A) Study IDcs (solid colored patches) on the western GIS with bounding boxes (semi-transparent squares) indicating corresponding domain used for bed transfer and admittance calculations. Imagery is from ArcGIS ERSI world imagery basemap. 500 m elevation contours (black) and ice surface velocity field (white arrows) are from sources cited in (Section 2.1). The black star in SE Greenland (submap) indicates the location of an additional region RSF we study that does not exhibit supraglacial streams. Information on all regions is in Table 1. (B) Ice surface and bed elevation from study region R1, with stream channels from study drainage network shown in black.

The Cryosphere Discuss., https://doi.org/10.5194/tc-2018-74
Manuscript under review for journal The Cryosphere
Discussion started: 17 May 2018

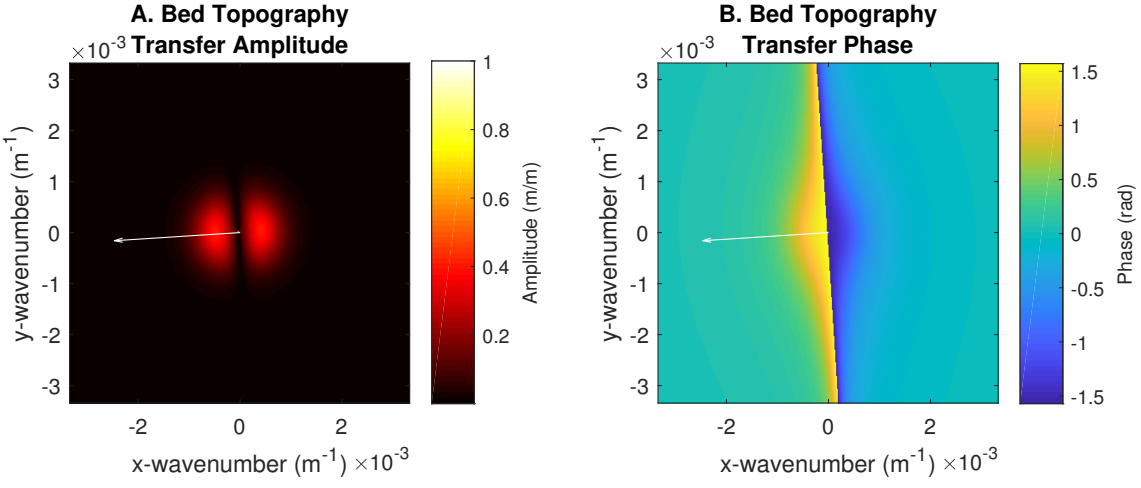

Figure 2. (A, B) 2D bed topography transfer function amplitude and phase, as defined in Appendix A1. White arrows in both plots indicate ice flow direction. Ice flow parameters used are from region R1 (Fig. 1.A, Table 1)with $\eta = 10^{14}$ Pa s and $C^{0*} = 11$.

The Cryosphere Discuss., https://doi.org/10.5194/tc-2018-74
Manuscript under review for journal The Cryosphere
Discussion started: 17 May 2018

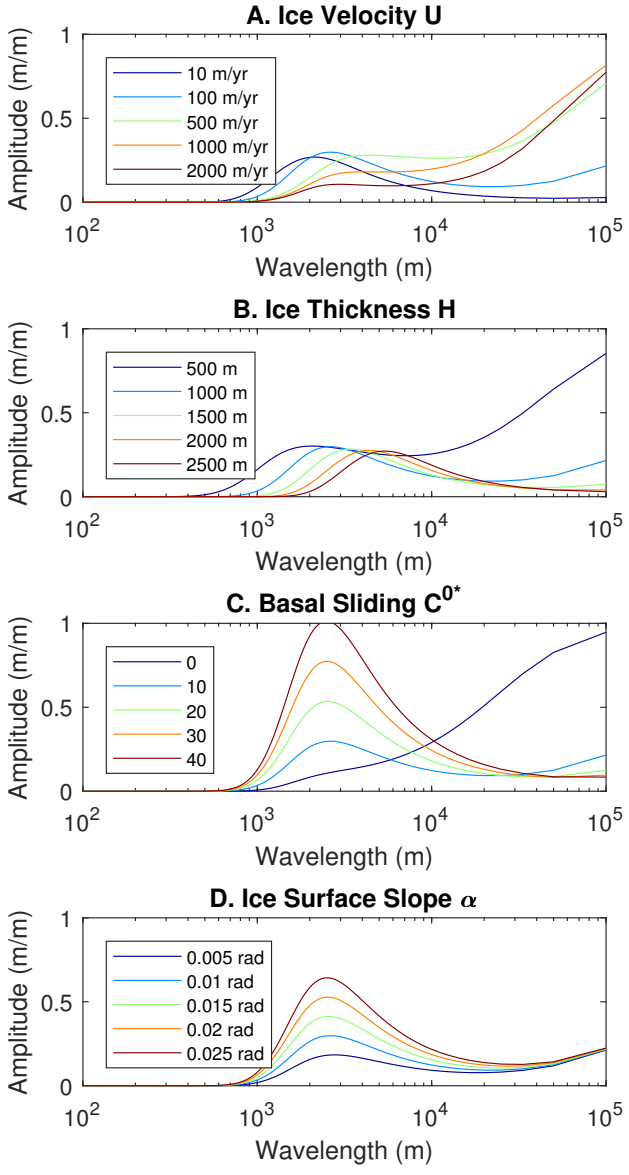

Figure 3. (A-D) Bed topography transfer function amplitudes in ice flow direction (along ice flowline). In all plots the parameters not otherwise indicated are: $U = 100$ m/yr, $H = 1000$ m, $C^{0*} = 10$, $\alpha = 0.01$ radians, and $\eta = 10^{14}$ Pa s.

The Cryosphere Discuss., https://doi.org/10.5194/tc-2018-74
Manuscript under review for journal The Cryosphere
Discussion started: 17 May 2018

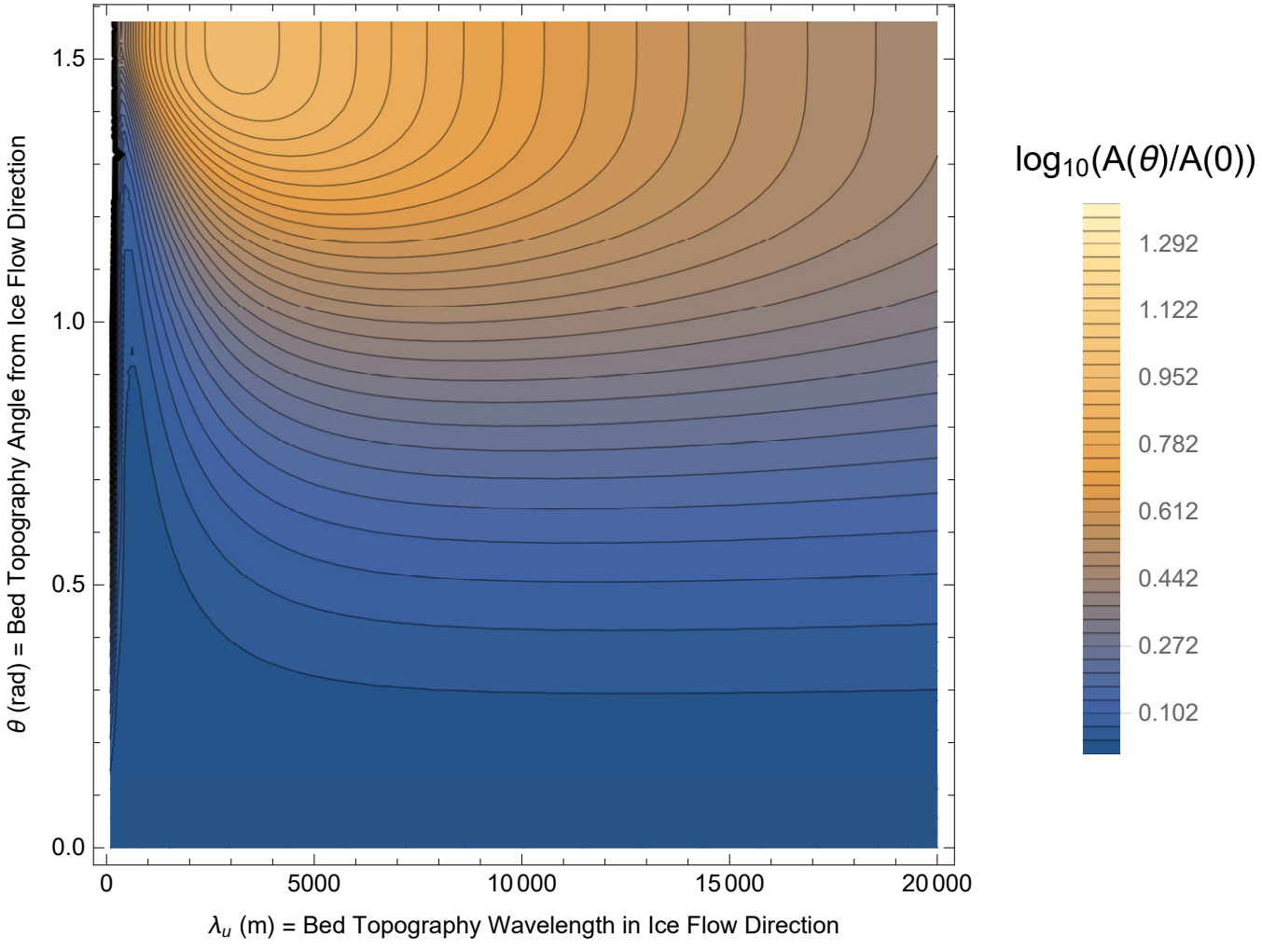

Figure 4. Effect of 2D bed topography on ice flowline bed topography transfer amplitude, defined in Appendix A2. $A(\theta)$ is predicted transfer amplitude for ice-flowline-equivalent bed topography aligned at angle θ from the ice flow direction, and $A(0)$ is the predicted flowline-only (equivalent to $\theta = 0$) transfer amplitude. Ice flow parameters used are from region R1 (Fig. 1.A, Table 1)with $\eta = 10^{14}$ Pa s and $C^{0*} = 11$.

The Cryosphere Discuss., https://doi.org/10.5194/tc-2018-74
Manuscript under review for journal The Cryosphere
Discussion started: 17 May 2018

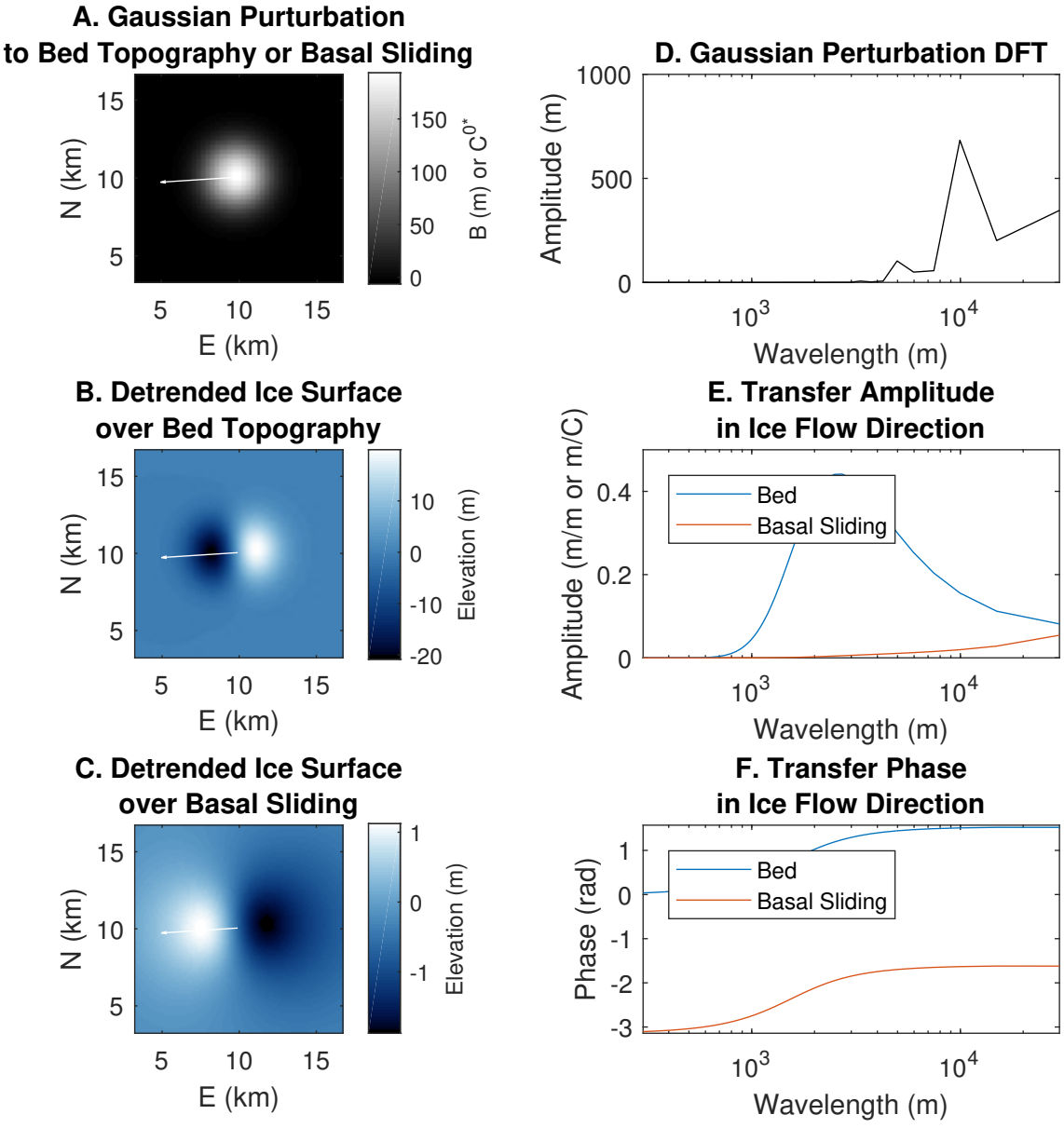

Figure 5. (A) Gaussian bed topography or basal sliding distribution. (B, C) Detrended predicted ice surface over basal perturbations. White arrows in (A, B, C) indicate ice flow direction. (D) The discrete Gaussian amplitude spectrum appears different from a continuous Gaussian amplitude spectra. (E, F) Transfer amplitudes and phases in ice flow direction. All ice flow parameters (other than bed topography and basal sliding) are from region R1 (Fig. 1.A, Table 1) with $\eta = 10^{14}$ Pa s and $C^{0*} = 11$ for the Gaussian bed topography test case (B).

The Cryosphere Discuss., https://doi.org/10.5194/tc-2018-74
Manuscript under review for journal The Cryosphere
Discussion started: 17 May 2018

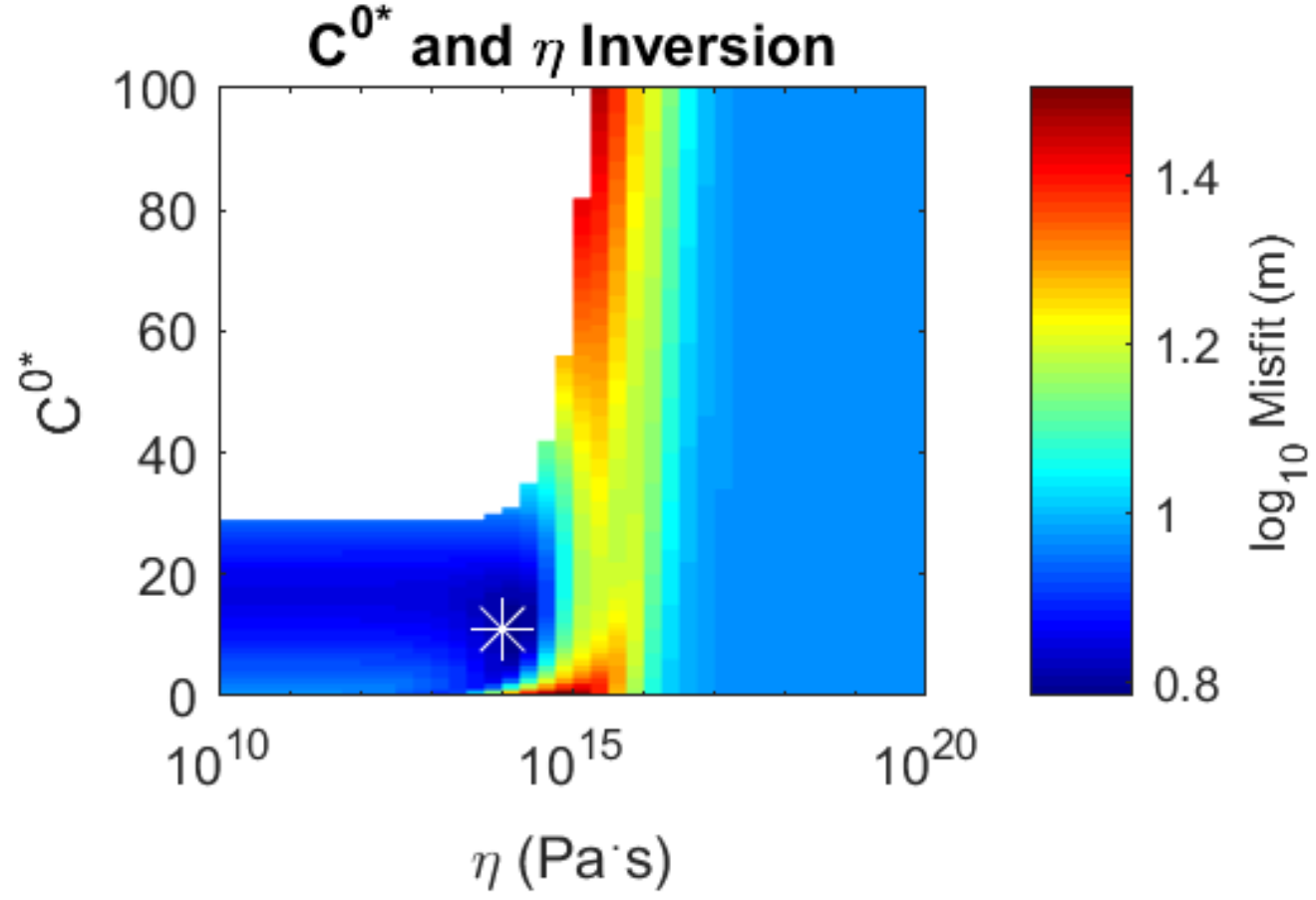

Figure 6. Misfit minimization for η and C^{0*} between the ice surface DEM and bed topography transfer predicted ice surfaces in study region R1 (Fig. 1.A, Table 1). White star indicates the location of minimum misfit, at $C^{0*} = 11$ and $\eta = 10^{14}$. Blank plot area is the region where parameters are nonphysical (resulting in transfer amplitudes > 1).

The Cryosphere Discuss., https://doi.org/10.5194/tc-2018-74
Manuscript under review for journal The Cryosphere
Discussion started: 17 May 2018

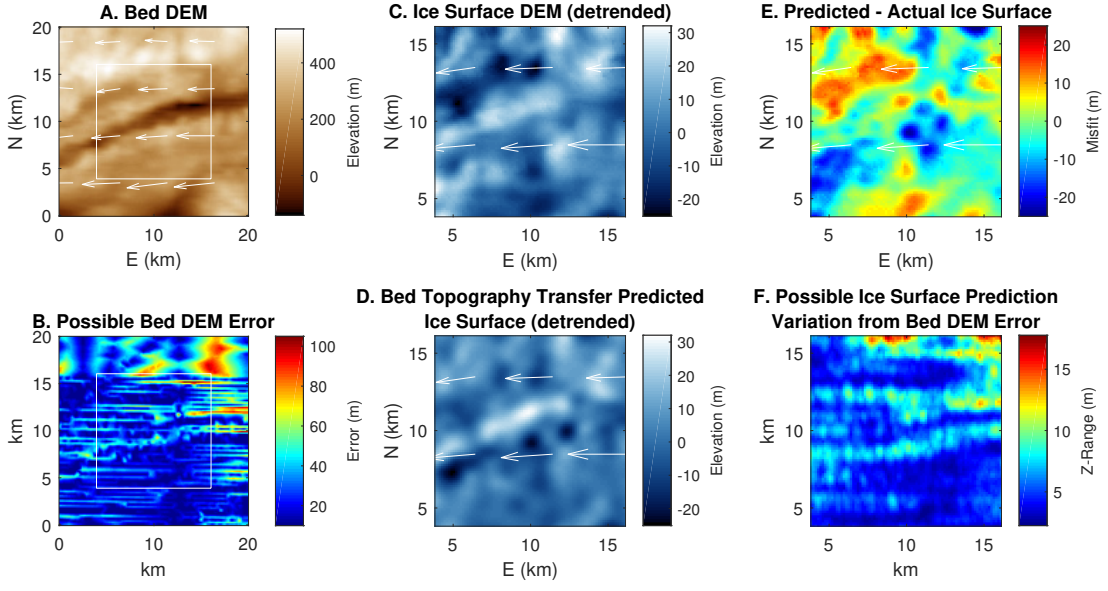

Figure 7. (A) Bed DEM from study region R1 (Fig. 1.A, Table 1). (B) Bed DEM error. White boxes in (A, B) indicate the region of the bed over which the ice surface is predicted. (C) Detrended ice surface DEM. (D) Detrended bed topography transfer predicted ice surface, with $\eta = 10^{14}$ Pa s and $C^{0*} = 11$. (E) Prediction misfit (subtraction between the actual (C) and predicted (D) ice surfaces). Though misfit is often large, ∼1-10 km scale topographic features are well predicted. (F) Potential effects of bed DEM error on ice surface predictions. White arrows in all plots indicate ice surface velocity field.

The Cryosphere Discuss., https://doi.org/10.5194/tc-2018-74
Manuscript under review for journal The Cryosphere
Discussion started: 17 May 2018

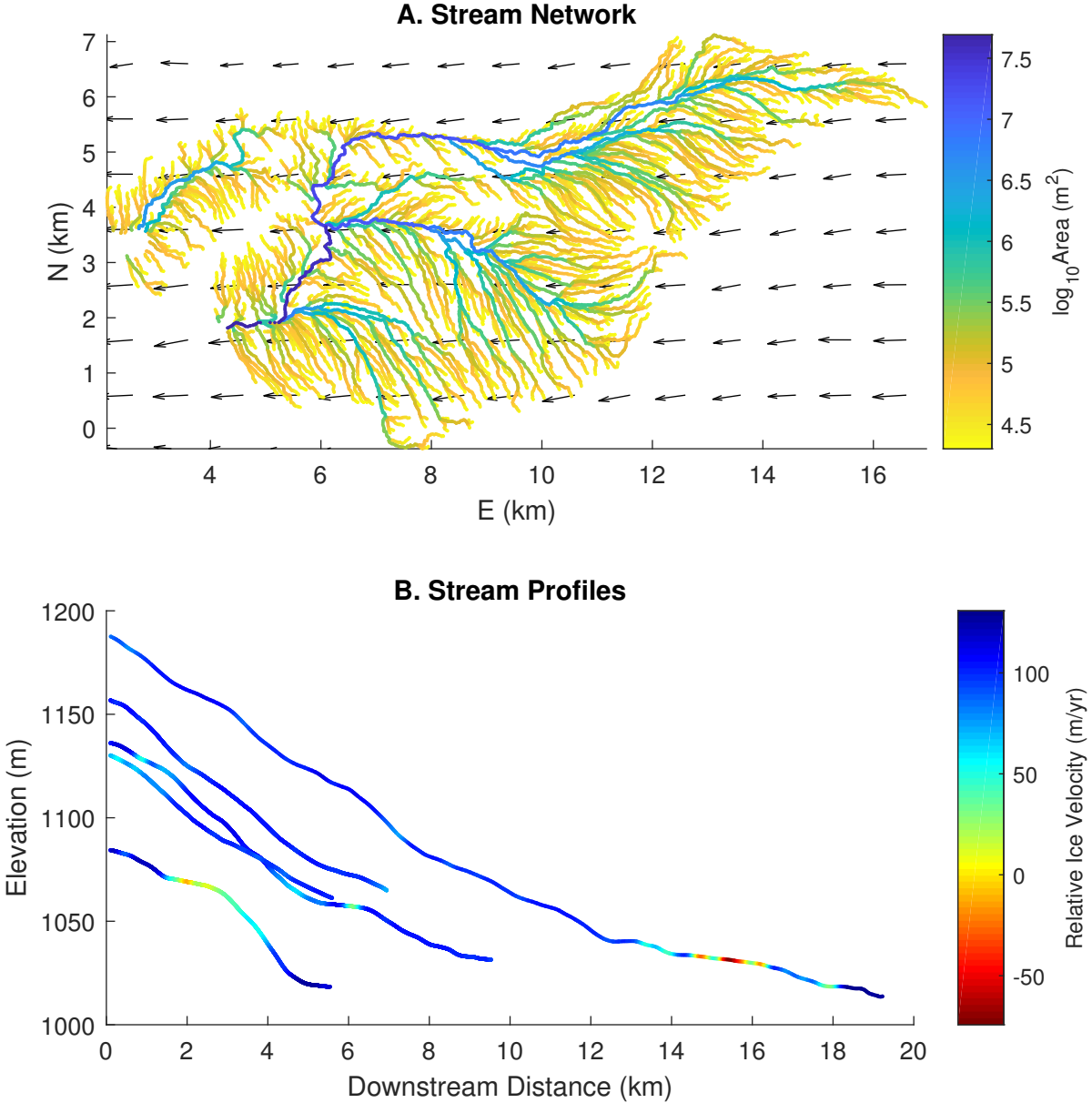

Figure 8. (A) Stream network obtained by flow routing from study region R1 (Fig. 1.A, Table 1) colored by accumulated upstream drainage area; black arrows indicate ice surface velocity field. (B) Smoothed longitudinal stream elevation profiles from the longest streams in this network, colored by the component of ice surface velocity in the direction of stream flow. Negative values indicate stream is flowing against ice flow direction.

The Cryosphere Discuss., https://doi.org/10.5194/tc-2018-74
Manuscript under review for journal The Cryosphere
Discussion started: 17 May 2018

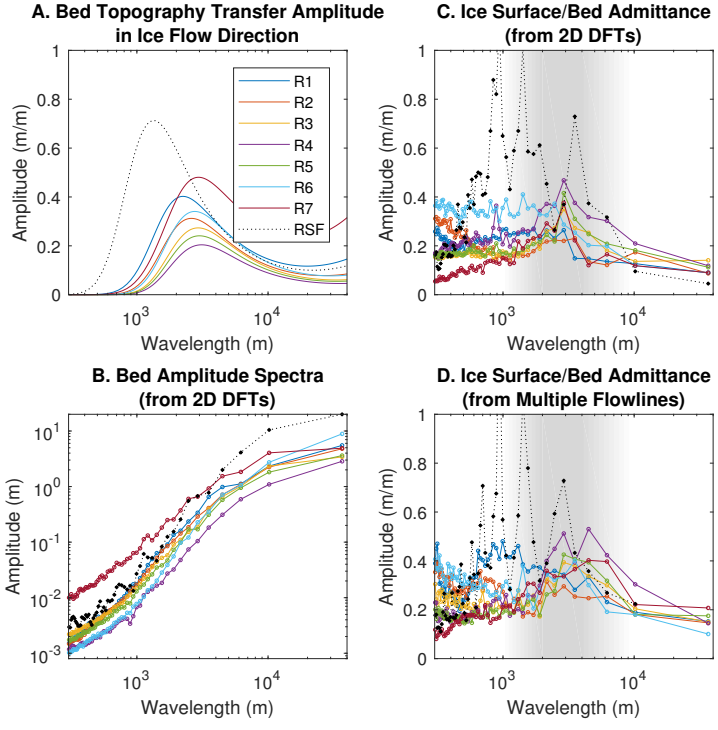

Figure 9. (A) Predicted bed topography transfer amplitudes from our seven study regions, plus a synthetic flow network from stream-free region RSF (Fig. 1.A, Table 1), with $\eta = 10^{14}$ Pa s and $C^{0*} = 11$ in all regions. (B) Bed topography amplitude spectra. (C, D) Two different calculations of empirical bed topography admittance to ice surface topography (Section 2.3.5). For all regions, both calculations of admittance generally match predicted transfer amplitudes at 1-10 km wavelengths.

The Cryosphere Discuss., https://doi.org/10.5194/tc-2018-74
Manuscript under review for journal The Cryosphere
Discussion started: 17 May 2018

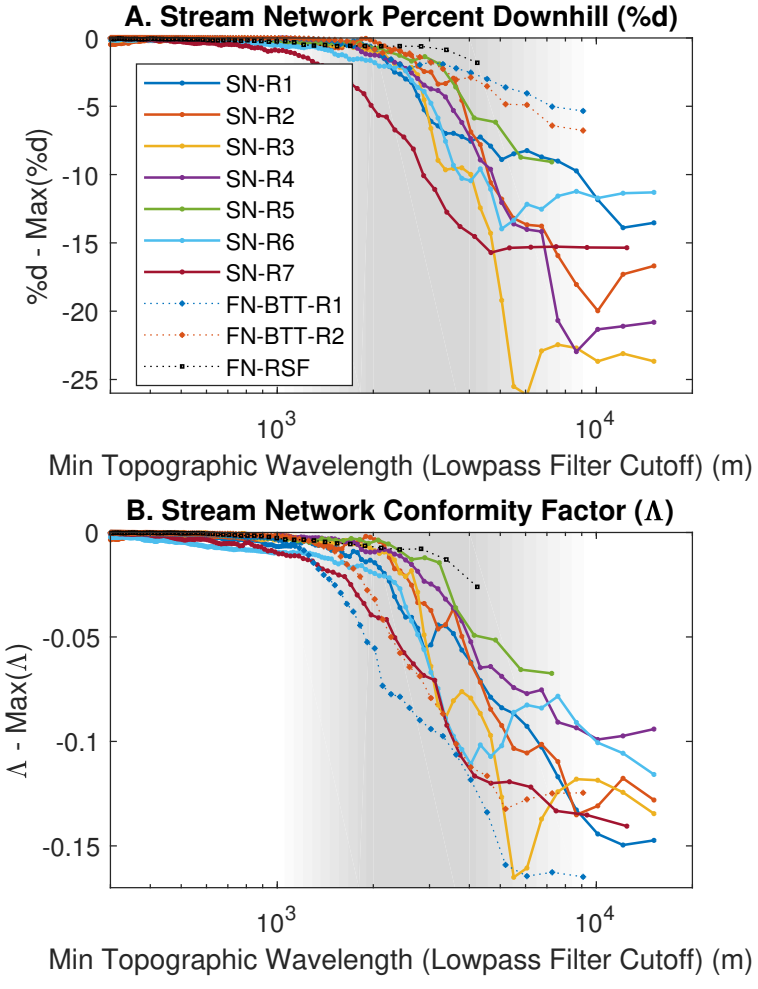

Figure 10. (A) Percent downhill $\%d$. (B) Conformity factor Λ. Values for both stream metric topographic conformity metrics are calculated in our seven study regions, plus synthetic flow networks from the stream-free study region FN-RSF and from two bed topography transfer predicted ice surfaces FN-BTT-R1 and FN-BTT-R2 (Fig. 1.A, Table 1). All values are normalized to the maximum values in each network due to the variability in plateau values of $\%d$ and Λ between networks. For all supraglacial stream networks and synthetic flow networks the only cutoff filter wavelengths over which $\%d$ and Λ change significantly are between ∼1-10 km.

The Cryosphere Discuss., https://doi.org/10.5194/tc-2018-74
Manuscript under review for journal The Cryosphere
Discussion started: 17 May 2018

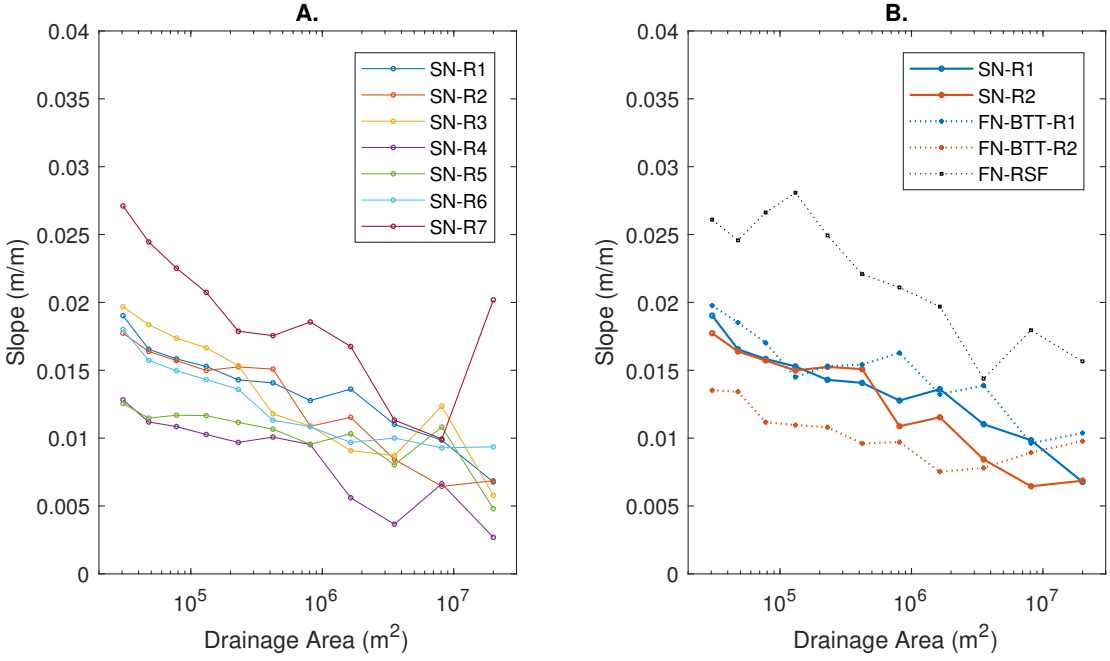

Figure 11. (A) Stream channel slope binned by accumulated upstream drainage area from supraglacial stream networks in our seven study regions (Fig. 1.A, Table 1). (B) Synthetic flow networks from a stream-free area of the GIS (FN-RSF) and from two bed topography transfer predicted ice surfaces (FN-BTT-R1 and FN-BTT-R2) with the corresponding supraglacial stream networks shown for comparison (solid blue and orange, identical to the curves in (A)).

The Cryosphere Discuss., https://doi.org/10.5194/tc-2018-74
Manuscript under review for journal The Cryosphere
Discussion started: 17 May 2018

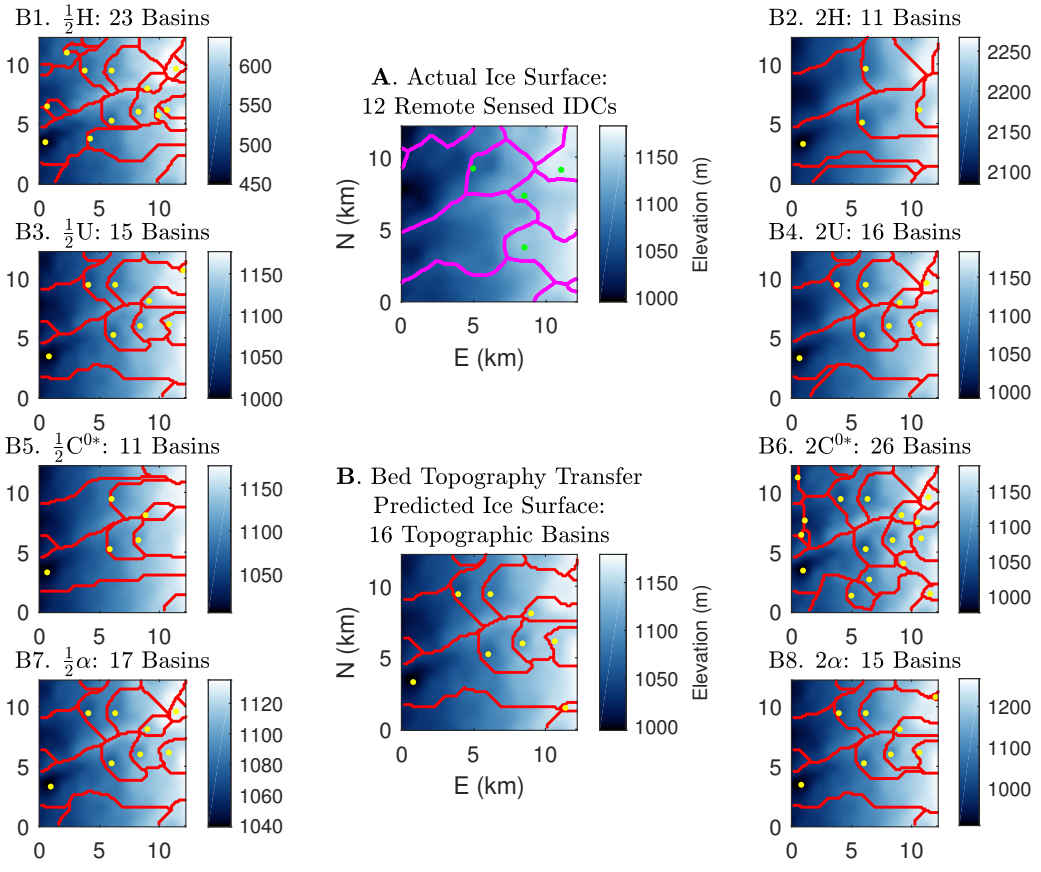

Figure 12. (A) IDCs (magenta outlines) and moulins (green dots) obtained from satellite images by (Yang and Smith, 2016). (B, B1-B8) Ice Surface topographic basins (red outlines) and local minima (yellow dots) on bed topography transfer predicted ice surfaces with various ice flow parameters. From study region R1 (Fig. 1.A, Table 1) with $\eta = 10^{14}$ Pa s and $C^{0*} = 11$. While the bed transfer predicted topographic basin configuration (B) is different from the IDC configuration (A), the basin densities are similar.

The Cryosphere Discuss., https://doi.org/10.5194/tc-2018-74
Manuscript under review for journal The Cryosphere
Discussion started: 17 May 2018

Table 1. Study region information (locations in Fig 1.A)

Study region	Ice thickness H (m)	Ice surface velocity U (m/yr)	Ice surface slope α (radians)	2015 Modeled melt rate M (mm water equivalent/yr)
R1	824	86	0.013	2107
R2	1075	87	0.009	1145
R3	1233	88	0.009	793
R4	1335	81	0.006	556
R5	840	214	0.017	1321
R6	1266	87	0.007	711
R7	1187	92	0.011	1552
RSF	586	30	0.018	392